



**Politecnico
di Torino**



**Université
Paris Cité**

INTERNATIONAL DOUBLE DEGREE PROGRAM

NanoQuad: Nanotechnologies and Quantum Devices

M A S T E R T H E S I S

**Rb₂Ti₂O₅ at the nanoscale:
characterization and charge transport**

Internship supervisor:

Dr. Clément Barraud

Academic supervisor:

Prof. Carlo Ricciardi

Candidate:

Valerio Digiorgio

Academic year 2021/2022

Contents

| | |
|---|-----------|
| Abstract | ii |
| 1 Chapter 1: Introduction | 1 |
| 1.1 Supercapacitors | 1 |
| 2 Chapter 2: Internship project and state of the art | 3 |
| 2.1 Project outline | 3 |
| 2.1.1 Presentation of the lab | 3 |
| 2.2 State of the art | 4 |
| 2.2.1 Recent characterization of RTO crystals | 4 |
| 2.2.2 Electrical characterization of $\text{Rb}_2\text{Ti}_2\text{O}_5$ | 6 |
| 2.2.3 Permittivity measurements | 7 |
| 2.2.4 Effects of water contamination | 8 |
| 3 Internship project | 10 |
| 3.1 Exfoliation | 10 |
| 3.1.1 Degradation over time | 11 |
| 3.2 Characterization: Raman spectroscopy and AFM | 12 |
| 3.2.1 Introduction on the techniques | 12 |
| 3.2.2 Setup: technical information | 13 |
| 3.2.3 Atomic force microscope measurements | 13 |
| 3.2.4 Raman spectroscopy measurements | 14 |
| 3.2.5 Raman spectra size-dependence | 16 |
| 3.3 Device fabrication | 19 |
| 3.3.1 Introduction on the techniques | 20 |
| 3.3.2 Design of the device | 21 |
| 3.4 Electrical measurements: preliminary results | 23 |
| 3.4.1 Measurement set-up | 23 |
| 3.5 $I - V$ measurements | 23 |
| 4 Conclusions | 26 |
| 4.1 Overview | 26 |
| 4.2 Future perspectives | 26 |
| Bibliography | 27 |

Abstract

Over the last century, the energy storage industry has continued to evolve, adapt, and innovate in response to changing energy requirements and advances in technology. Currently, energy storage systems are available for various large-scale applications and are classified into different types. In particular, electrical energy storage systems (EES) in terms of electrochemical capacitors (ECs) and batteries have demonstrated great potential.

In the last decades, research has focused on the development of all aspects of EES, electrolyte material among them. The perovskite-derived material $\text{Rb}_2\text{Ti}_2\text{O}_5$ (RTO), has been recently found to display very interesting dielectric and conduction properties, showing an equivalent relative permittivity up to 10^9 at room temperature, high ionic conductivity (up to $10^{-3} \text{ S}\cdot\text{cm}^{-1}$) and very low electronic conductivity ($\sim 10^{-9} \text{ S}\cdot\text{cm}^{-1}$). The remarkable properties of this material make it interesting for applications, in particular for its use as a solid electrolyte for the realization of advanced energy storage systems.

Here, I present the first approach to study RTO at the nanoscale, in order to characterize its properties and investigate the charge transport. Having a lamellar structure, RTO is a promising candidate for micro-mechanical exfoliation to obtain thin samples.

In this work, first a review of the previous results obtained for bulk RTO crystals is described in the State of the art section, then, a detailed study of the physical and electrical properties of RTO nanocrystals is presented.

Samples are obtained after micro-mechanical exfoliation through scotch-tape technique. Characterization of the exfoliated flakes is carried out by performing AFM (Atomic Force Microscopy) and Raman spectroscopy measurements. Devices are fabricated in cleanroom by photolithographic process, e-beam evaporation and hot pick-up transfer technique. Finally, electrical measurements are performed to extract information on the charge transport in RTO nanocrystals.

Nanocrystals are feasibly obtained through scotch-tape exfoliation technique and mostly present a thickness close to 300 nm. The already known hygroscopic character of the material is also found in exfoliated RTO. Water absorption tends to deteriorate the crystals over time, but it is responsible for the modification of the RTO Raman spectrum and for the ionic conduction. The conductivity of nanocrystals is comparable to that of bulk RTO and in agreement with results of previous works.

This work represents the first approach to the study of $\text{Rb}_2\text{Ti}_2\text{O}_5$ at the nanoscale. Exfoliated nanocrystals have shown similar properties to those of bulk RTO, concerning water absorption and electrical conduction. The obtained results strengthen the theory about the cruciality of water in determining the properties of this material. Further investigation will be needed in order to determine quantitative relations between the water content inside the material and its physical and electrical properties, and to fully understand the charge transport in RTO.

1 Chapter 1: Introduction

In today's world, there is a continuous global need for more energy which, at the same time, has to be cleaner than the energy produced from the traditional generation technologies. The penetration of renewable energy sources and of other forms of potential distributed generation sources is increasing worldwide. These types of energy sources often rely on the weather or climate to work effectively, exploiting, for example, solar power, wind power and hydroelectricity in its many forms.

Conventional and renewable sources are integrated with electrical energy storage systems (EESSs) to carry out the supply of power for both large and small scale power grids.

Although renewable energy generation has some indisputable advantages, it presents new challenges associated with its variability and uncertainty. The output of the traditional methods is easy to adjust according to the power requirements. The new energy sources may exhibit large fluctuations in power output caused by natural conditions in monthly or even annual cycles. Similarly, the demand can vary monthly or annually.

Current EESSs are not able to efficiently deliver the necessary power at fast rates to avoid these fluctuations. Therefore, in order for these new sources to become completely reliable as primary sources of energy, energy storage is a crucial factor. Essentially, energy from these sources must be stored at their peak availability and utilizes the stored energy at their downtime. Renewable energy conversion represents just one of the numerous fields of application of advanced energy storage systems. They are becoming increasingly crucial devices especially for high power applications, spanning almost all the fields where electrical energy is in the picture, automotive being now among the most popular with the huge growth of the electric vehicles market.

1.1 Supercapacitors

One of the most promising storage technologies is represented by supercapacitors, also called ultracapacitors. They differ from conventional capacitors due to their fast charge–discharge rates, longer life cycle, high power, and high energy density. There are two types of supercapacitors depending on the charge storage mechanism. The first type is an electrical double-layer capacitor (EDLC) that stores electrical energy by accumulating charges at the electrode–electrolyte interface forming a double layer of charges. The second type of supercapacitor is known as a pseudocapacitor as it uses faradaic reactions to store electric energy. Also hybrid type devices exist, formed by a combination of EDLC and pseudocapacitor.

Supercapacitors are governed by the same fundamental equations as traditional capacitors in which capacitance can be derived from the conventional capacitance, which is given by

$$C = \frac{\epsilon_o \epsilon_r A_e}{d}$$

where A_e = geometric surface area of the electrode; ϵ_o = permittivity of free space; ϵ_r = relative permittivity of the dielectric material; and d = distance between two oppositely biased electrodes. The amount of energy stored can be increased by either increasing the capacitance or the voltage stored on the capacitor. The stored voltage is limited by the voltage-withstand-strength of the dielectric (which impacts the distance between the plates). Capacitance can be increased by increasing the area of the plates, increasing the permittivity, or decreasing the distance between the plates.

Considering an EDLC-type supercapacitor, a potential difference is generated at the electrode-electrolyte interface upon application of an electric potential to the electrodes. The electrode-electrolyte interface incorporates a double layer formed between the electrolyte ions and electronic charges on the electrode. In this case, d in the preceding

equation is the double layer thickness, which is very small. Since the capacitance and energy of a capacitor are inversely proportional to d , supercapacitors are capable of storing large amounts of energy.

To achieve the highest potential, research has focused on the improvement of all three aspects of supercapacitors: electrode material, electrolyte material, and the architectural design of the materials.

Electrolyte plays a critical role in supercapacitor performance. A good electrolyte offers a wide voltage window, high electrochemical stability, high ionic concentration and conductivity. The electrolytes for electrochemical supercapacitors are classified into various categories. A first classification concerns aqueous, organic, ionic liquid, and solid-state electrolytes.

Solid-state electrolytes (SSEs) have been attracting the scientific community's attention in the last decade. These electrolytes provide significant advantages, such as the absence of leakage and separators for devices and safety for users. Inorganic solid electrolytes could also support operation at low and high temperatures (for example, -50 to 200 °C or higher) in which conventional liquid electrolytes would freeze, boil or decompose.

To date, a variety of solid materials have been investigated as SSEs, perovskite-type SSEs among them.

The perovskite-derived material $\text{Rb}_2\text{Ti}_2\text{O}_5$ (in the following RTO), belonging to the $\text{M}_2\text{Ti}_2\text{O}_5$ (with $\text{M} = \text{Li}, \text{Na}, \text{K}, \text{Rb}, \text{Cs}, \text{Fr}$) family, whose structure was identified in the 1960's[1,2], has been recently found to display very interesting dielectric properties, showing an equivalent relative permittivity up to 10^9 at room temperature. This is three to four orders of magnitude above competitive materials and was attributed to ionic motion[3].

The remarkable properties of this material make it interesting for applications, in particular, for the realization of supercapacitors for energy storage [4,5]. Its high ionic conductivity and very low electronic conductivity are particularly interesting for its use as a solid electrolyte[3].

2 Chapter 2: Internship project and state of the art

2.1 Project outline

My research project, in the context depicted so far, aims at investigating the properties of RTO down to the nanoscale and fabricating devices for the characterization of its charge transport mechanism and properties.

The project outline is schematically depicted in Fig.1.

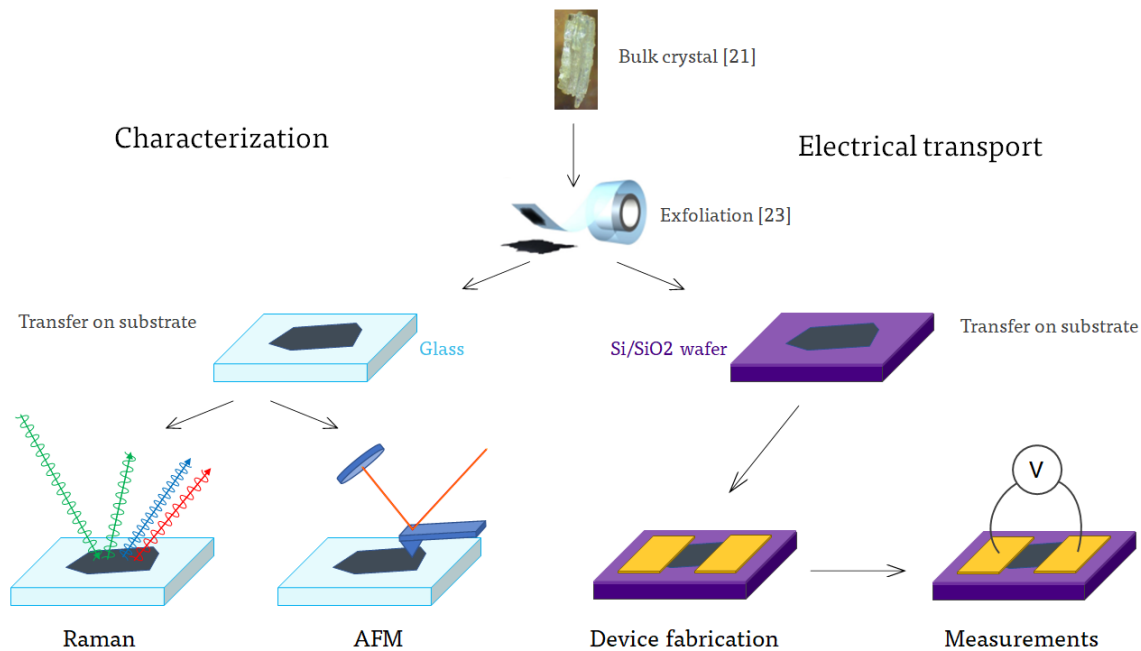


Figure 1: Project outline.

The first step consists in performing a micro-mechanical cleavage of the bulk RTO crystals via scotch-tape dry exfoliation technique. Depending on the analysis to be eventually carried out, the exfoliated material is transferred on a glass substrate (microscope slide) or on an oxidized Si wafer. In the former case, the sample is characterized through Raman spectroscopy and AFM (Atomic Force Microscope) measurements, in the latter device fabrication follows, with the deposition of gold contacts to electrically connect the material and perform electrical measurements.

2.1.1 Presentation of the lab

My internship is conducted at the *Matériaux et Phénomènes Quantiques* (MPQ) lab, in the TELEM group. The laboratory specializes in the study of frontier quantum materials and in the development of novel quantum devices. These activities rely on a large spectrum of theoretical and experimental expertise in material physics, transport and optics, and technological platforms of clean-room fabrication, spectroscopy and high-resolution electronic microscopy. Research activity in our team is focused on charge, spin and heat transport in low-dimensional systems such as 2D materials and molecular layers, and in hybrid structures coupling these materials, such as graphene or functionalized carbon nanotubes. We also study the properties of 2D material stacked in van der Waals heterostructures and explore new technological approaches using graphene and/or carbon nanotubes as "contacts" on molecules towards fully carbon-based electronics.

My work is done in collaboration with the LPEM (*Laboratoire de Physique et d'Etude des matériaux*) lab at ESPCI.

2.2 State of the art

The ternary titanium oxides denoted by $M_2Ti_nO_{2n+1}$ with $M = \text{Li, Na, K, Rb, Cs, Fr}$, called the Andersson–Wadsley type alkali titanates [12] are known for their interesting properties [13]. In particular, some of them present ferroelectric phase transitions, with remarkably high Curie temperatures [14]. $M_2Ti_2O_5$ (MTO) compounds (Andersson–Wadsley compounds with $n = 2$) exhibit a fivefold coordination for titanium, which originally came as a surprise because Ti^{4+} mostly tends to adopt an energetically more stable sixfold coordination [15]. The MTO compounds offer a certain interest for chemistry because of their oxidation abilities [17,18] but their electrical properties have not been investigated until recently [3]. Little information has been reported to date in the literature concerning the $Rb_2Ti_2O_5$ (RTO) compound. Early structural investigations were made on $K_2Ti_2O_5$ (KTO), where the space group is reported to be $C2/m$ and, more generally, on the MTO family [12,15,16]. Two early reports exist on the synthesis and crystal structure of $Rb_2Ti_2O_5$, which was stated to be consistent with the $C2/m$ space group [19,20].

2.2.1 Recent characterization of RTO crystals

The unit cell of RTO is shown in Fig.3. This two-dimensional structure consists in alternate layers of Ti–O (namely $Ti_2O_5^{2-}$) and Rb (namely Rb^+) atoms stacked along the c axis.

The $(Ti_2O_5)^{2-}$ planes are composed of staggered upside and downside oxygen pyramids (see Fig.4). The Ti atoms (in blue) are at the center of these slightly tilted square-based-pyramids and are therefore surrounded by five oxygen atoms (in red).

These planes are separated by the Rb atoms (in pink). This structure is in excellent agreement with High-resolution transmission electron micrographs (HRTEM), shown in Fig.2 [21], as clarified by the inset showing an enlargement of a particular region of the image. The crystals, as revealed by scanning electron microscopy (SEM) images in Fig.5 [21], clearly show a lamellar structure making

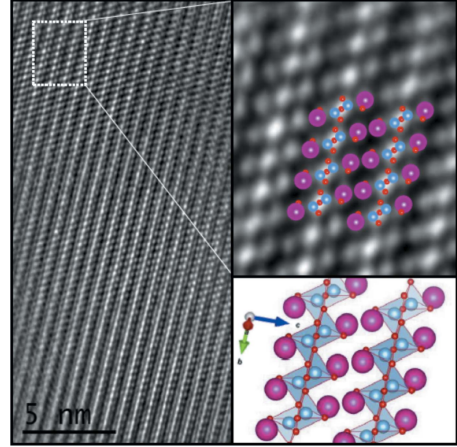


Figure 2: High-resolution transmission electron micrograph of an $Rb_2Ti_2O_5$ sample along the $[110]$ axis. [21]

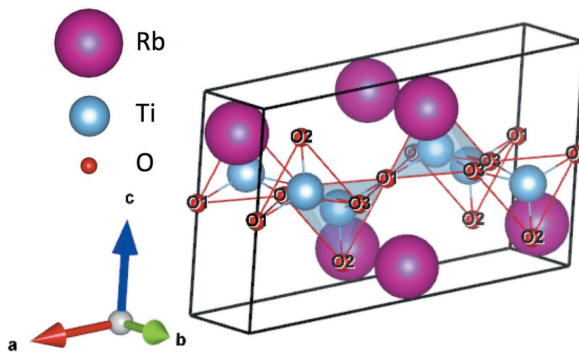


Figure 3: Structure of $Rb_2Ti_2O_5$ unit cell. [21]

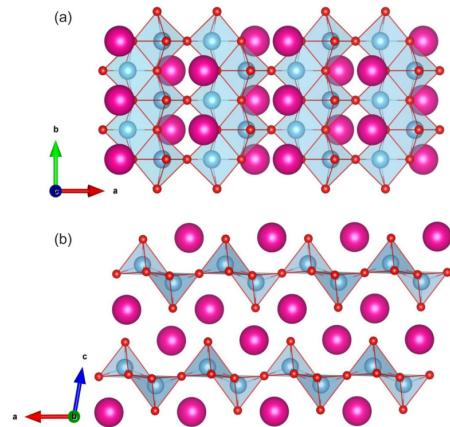


Figure 4: $Rb_2Ti_2O_5$ crystal structure: (a) view along the c axis; (b) view along the b axis, evidencing the lamellar structure. [21]

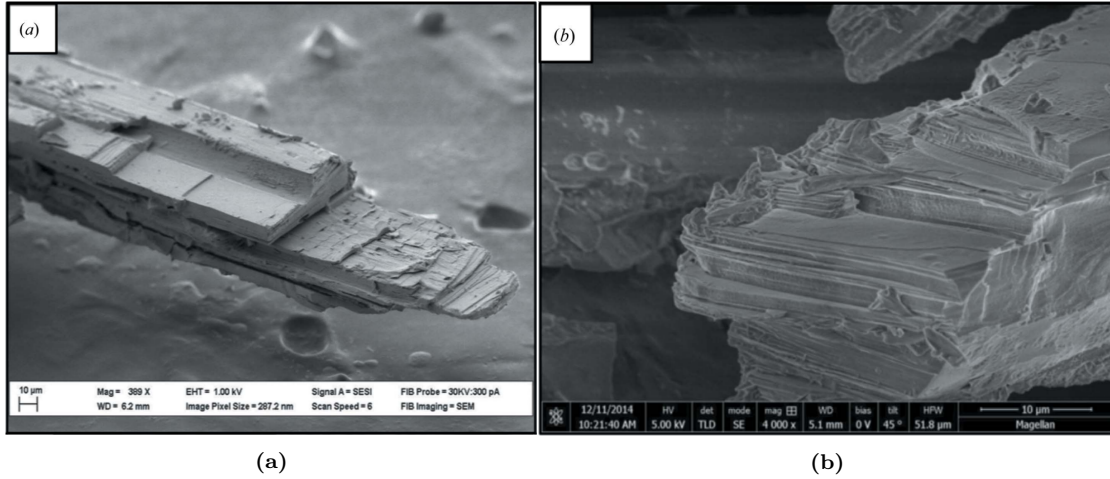


Figure 5: Scanning electron micrographs of two as-grown $\text{Rb}_2\text{Ti}_2\text{O}_5$ crystals: (a) magnification $\times 369$ and (b) magnification $\times 4000$. The lamellar structure along the ab planes is clearly evidenced. [21]

them easily cleavable along the ab planes. This aspect is of great relevance for obtaining a very thin sample.

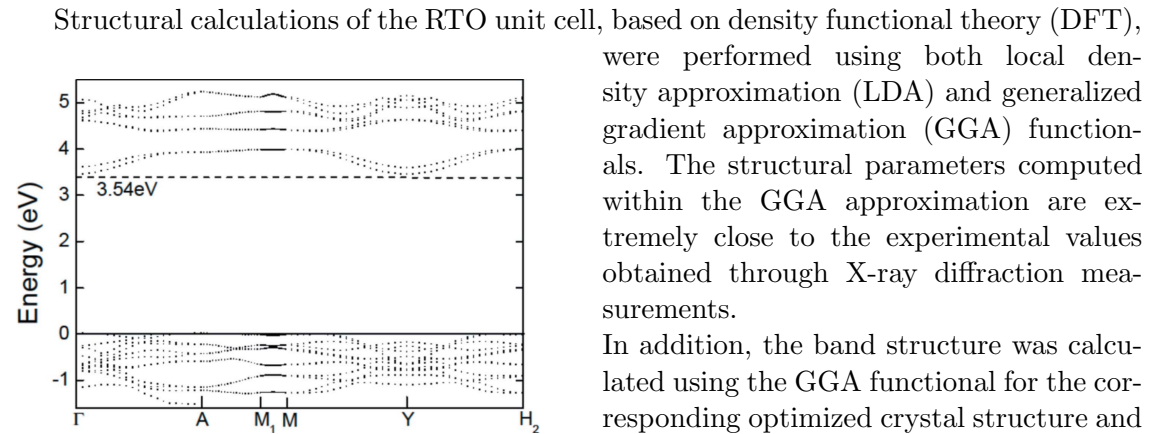


Figure 6: Band structure of $\text{Rb}_2\text{Ti}_2\text{O}_5$ calculated with GGA functional. [21]

Structural calculations of the RTO unit cell, based on density functional theory (DFT), were performed using both local density approximation (LDA) and generalized gradient approximation (GGA) functionals. The structural parameters computed within the GGA approximation are extremely close to the experimental values obtained through X-ray diffraction measurements.

In addition, the band structure was calculated using the GGA functional for the corresponding optimized crystal structure and the result is shown in Fig.6 [21]. A gap of at least 3.54 eV, which is likely to be underestimated as usual in the DFT-GGA, attests to the insulating nature of the RTO crystal.

DFT calculations based on density functional perturbation theory were also performed for finding the phonon modes frequencies and predicting the RTO Raman spectrum [21]. The outcome of the calculations, with both LDA and GGA approximations, are compared

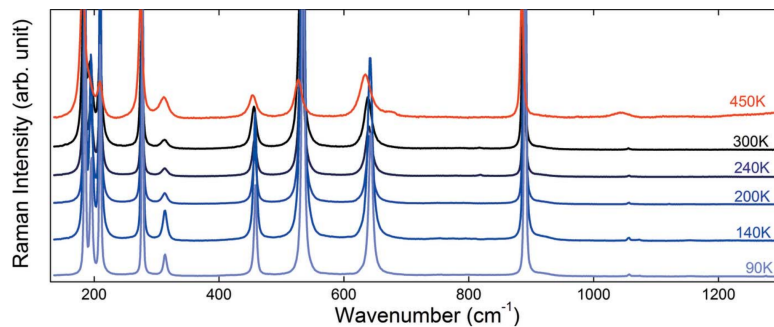


Figure 7: Experimental Raman spectra obtained on an $\text{Rb}_2\text{Ti}_2\text{O}_5$ as-grown crystal as function of the temperature between 180cm^{-1} and 1300cm^{-1} . [21]

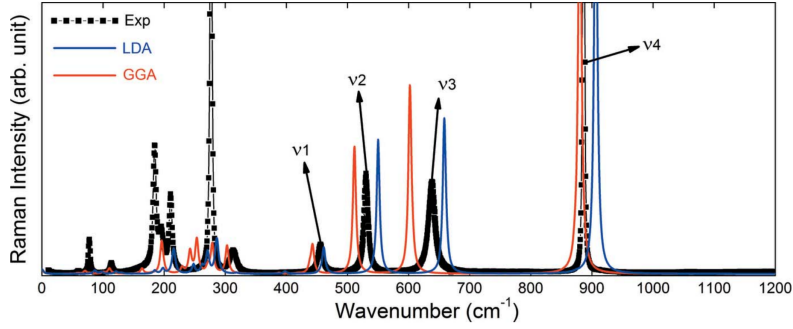


Figure 8: Experimental and simulated Raman spectra for $\text{Rb}_2\text{Ti}_2\text{O}_5$. The black squares represent the experimental Raman spectrum data points, between 10cm^{-1} and 1200cm^{-1} , measured at 300 K. [21]

with the results of Raman spectroscopy measurements (Fig.8 [21]) performed on RTO crystals over the range of temperature 90–450 K (see Fig.7 [21]). The agreement is very good, as may be seen for the ν_1 , ν_2 , ν_3 and ν_4 phonon modes, taking into account the tendencies of LDA and GGA to respectively overestimate and underestimate the phonon frequencies. This confirms that the structure is consistent with the centrosymmetric $C2/m$ space group.

2.2.2 Electrical characterization of $\text{Rb}_2\text{Ti}_2\text{O}_5$

Recent work on RTO has demonstrated superionic conduction properties stemming from the electrolytic nature of the material due to ionic migration. The nature of the ionic transport is not fully understood, but, as far as it is known, water contamination represents a crucial factor. It is already established that lamellar oxides such as MTO are prone to water intercalation [29,30,31]. RTO crystals are shown to spontaneously hydrate when exposed to ambient atmosphere [28]. Part of the intercalated water molecules experiences ion dissociation. The dielectric constant and the electrical polarization were shown to reach unprecedented values such as 10^9 and $0.1\text{ C}\cdot\text{cm}^{-2}$, respectively, which is attributed to high ionic conduction of the order of $10^{-3}\text{ S}\cdot\text{cm}^{-1}$, together with extremely low electronic conductivity (lower than $10^{-8}\text{ S}\cdot\text{cm}^{-1}$) [3]. These two combined properties make the material simultaneously a superionic conductor and an extremely good dielectric, promoting this material as an ideal candidate for applications, especially in supercapacitors.

Several crystals of $\text{Rb}_2\text{Ti}_2\text{O}_5$ were isolated and contacted using silver wire two-probe contacts glued with carbon paint [3]. The electrical resistivity of the as-grown $\text{Rb}_2\text{Ti}_2\text{O}_5$ crystals was found to be extremely high (typically above $10^8\ \Omega\cdot\text{cm}$). However, after annealing under helium atmosphere at 400 K for a couple of hours, the resistance at 300 K went down by at least 4 orders of magnitude. Hereafter this process is referred to as “activation” of the material. The material could be “deactivated” by annealing under oxygen atmosphere, which tends to indicate that the mechanisms at play are redox processes and that O_2 vacancies may play a crucial role in determining RTO properties.

In Fig.9 is displayed the $I - V$ curve of an “activated” single crystal of dimensions

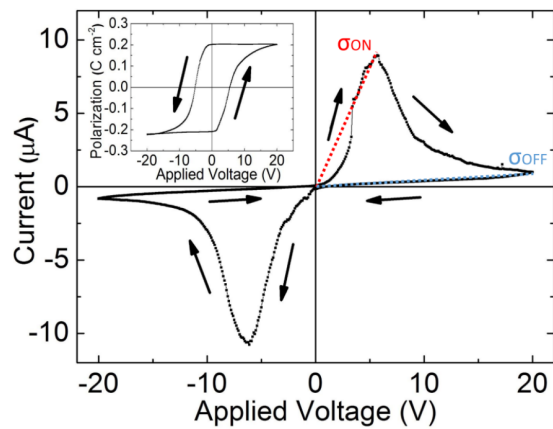


Figure 9: Current versus applied voltage ($\omega = 1.2\text{ mHz}$) for a single crystal at 260 K. Inset: Corresponding polarization versus applied voltage. [3]

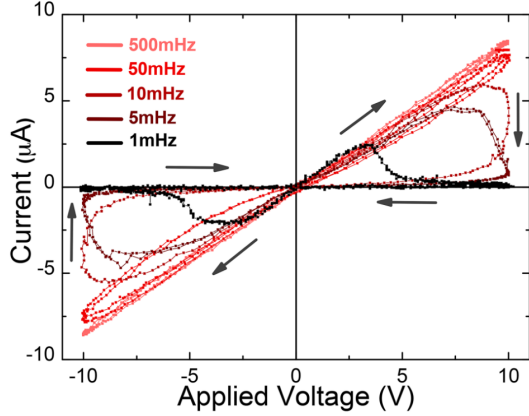


Figure 10: $I-V$ curves for $\text{Rb}_2\text{Ti}_2\text{O}_5$ single crystal under room conditions for frequencies ranging from 1 mHz to 500 mHz. [22]

paste at both ends of the elongated crystals. The entire system was then annealed at 400 K under room atmosphere to polymerize the carbon paste. Once connected, to activate the electrical transport properties, the crystals were annealed under vacuum at 400 K for two hours. The outcomes of the measurements (Fig.10) show non-linear non-transverse (the two branches do not cross at the origin) hysteretic loops that are pinched in zero. When the frequency of the applied voltage reaches 500 mHz, the $I-V$ curve shows an ohmic behavior with a single-valued conductivity of about $10^{-4} \text{ S}\cdot\text{cm}^{-1}$.

2.2.3 Permittivity measurements

The dielectric constant as a function of temperature and frequency was also investigated [3], leading to the results displayed in Fig.11. In Fig.11a are plotted the real and imaginary parts of ϵ_r as a function of frequency for three different temperature values. While the curves are featureless at 170K and 400 K, the curves at 300 K exhibit two distinct regimes separated by a cutoff frequency ω_C of about 10 Hz. Remarkably enough, below this cutoff frequency, the imaginary and real parts of the dielectric constant seem to converge to the same frequency behavior approximately following $1/\sqrt{\omega}$. This observation is typical of ionic diffusion processes that can be modeled by Warburg impedances [3]. Fig.11b, displaying Cole-Cole [13,14] plots acquired at 260 K and 300 K, gives a better picture of the diffusion mechanism. Below 5–10 Hz, the linear relation typical of the ionic

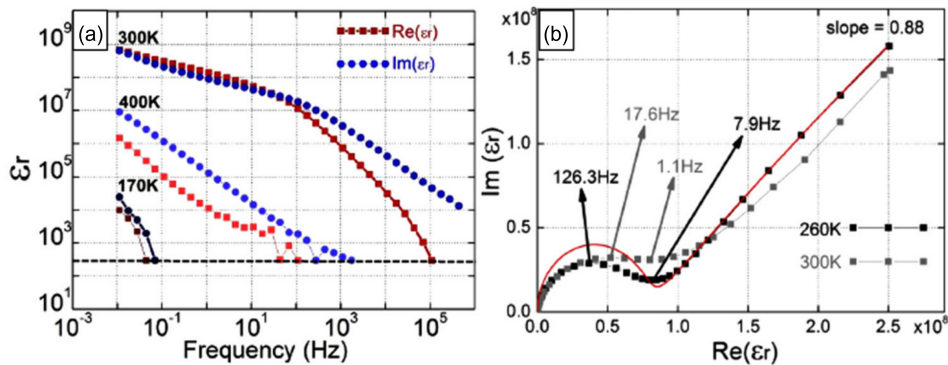


Figure 11: (a) $\text{Re}(\epsilon_r)$ (red squares) and $\text{Im}(\epsilon_r)$ (blue dots) curves vs frequency at 170, 300, and 400 K. (b) Cole-Cole plot of the permittivity at 300 K. Red line: Electrical model pictured in Fig.12a, with parameters $R_I = 3 \times 10^5 \Omega$, $C_{max} = 1.5 \times 10^{-6} \text{ F}$, $C_w = 30.7 \times 10^{-9} \text{ F}$, $W = 5 \times 10^7 \text{ F}\cdot\text{s}^{-1/2}$. [3]

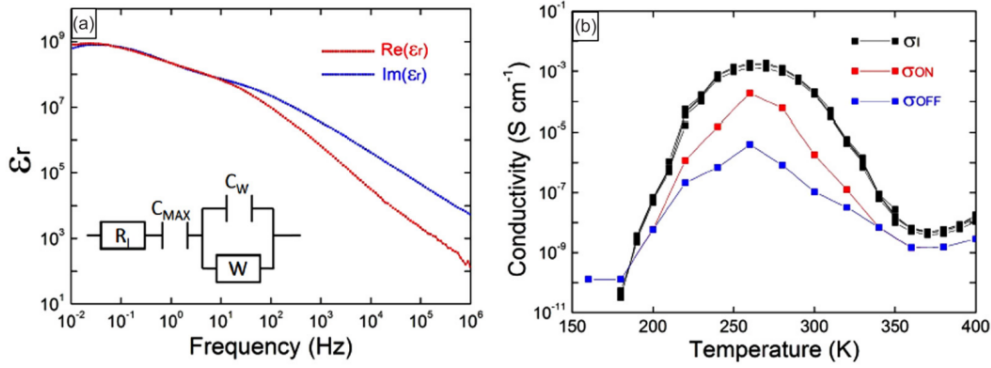


Figure 12: (a) $\text{Re}(\epsilon_r)$ and $\text{Im}(\epsilon_r)$ as function of frequency at 300 K under ambient pressure and temperature conditions. Inset: Equivalent electrical model for the samples, accounting for the Cole-Cole plots of Fig.11d. (b) Ionic conductivity σ_I extracted from the high-frequency value of $\text{Re}(\epsilon_r)$ plotted as a function of temperature. σ_{ON} and σ_{OFF} are extracted from the $I - V$ curves as shown in Fig.9. [3]

diffusion is clearly evidenced through the existence of a constant phase element (the slope of the line is close to 1, precisely 0.9).

In Fig.12a is displayed another permittivity curve obtained under ambient atmosphere as a function of frequency [3]. In this case, the “Warburg” impedance element is slightly modified and a saturation effect for $\text{Re}(\epsilon_r)$ appears at low frequency. This effect corresponds to the accumulation of ionic species on the edges of the sample. The curves indeed exhibit three distinct regimes: the saturation at low frequency, the Warburg regime with slope $-1/2$, and a conduction regime where $\text{Im}(\epsilon_r)$ has a slope -1 . An equivalent electrical model for the samples can be proposed, which is pictured in the inset of Fig.12a. In this equivalent circuit model, C_{max} is the maximal capacitance that can be attained by the sample. This corresponds to the maximum of dielectric constant $\epsilon_r \approx 10^9$. The polarization is then maximal. This is attained at extremely low frequency and for sufficient value of the electric field, where the crystal behaves like a double-layer supercapacitor. The second capacitance C_W in parallel with the Warburg impedance element determines, together with R_I , the cutoff frequency $\omega_C = 1/R_I C_W$. The latter separates the Warburg regime, where the diffusion layer is experienced by the system, from the regime of freely moving ions characterized by the resistivity R_I at high frequency, when edge effects are not relevant anymore. This electrical model accounts reasonably well for the Cole-Cole plot of Fig.11b. The conductivity $\sigma_I = R_I^{-1}$ is plotted in Fig.12b together with σ_{ON} and σ_{OFF} extracted from the $I - V$ curves as a function of temperature. The anomalously high value of the polarization suggests the existence of a macroscopic dipole in the sample related to ion displacements in the material. It is established that this dipole is maximal between 200 K and 320 K, precisely in the range where the ionic conductivity extracted from the equivalent permittivity measurements is maximal. This macroscopic dipole can only exist provided the electrodes are ion blocking. This implies that charge transfer at the electrode interfaces is negligible; the carriers are confined in the sample and accumulate at the edges.

2.2.4 Effects of water contamination

Thermogravimetric analyses (TGA) were performed on an as-grown RTO powder to measure the weight gain of the sample during rehydration [28]. It was first heated at 550°C under oxygen for 4 hours to ensure a complete elimination of water. Then, it was cooled down to room temperature, and the measurement chamber was opened to measure the weight gain.

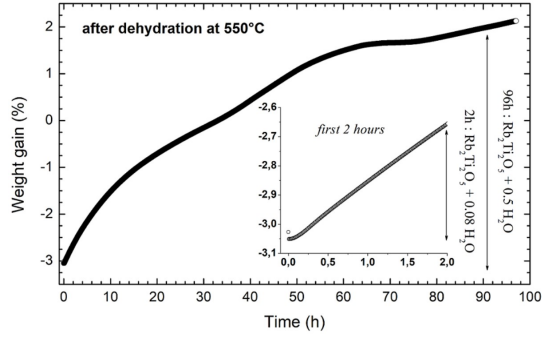
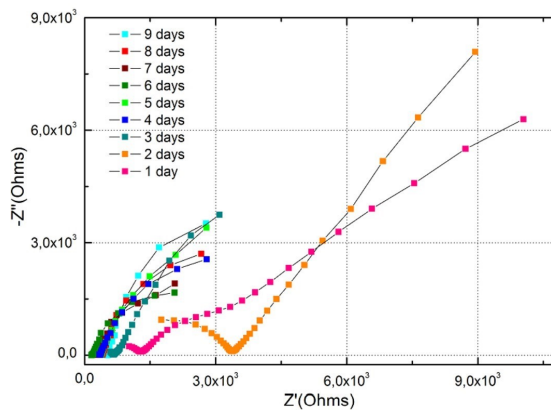


Figure 13: Weight gain observed during the rehydration of a sample, previously dehydrated at 550°C during 4 h. [28]

box to minimize exposure to ambient atmosphere. After measuring the 350°C-dehydrated RTO sample inside a glove box, the sample was taken out and dielectric measurements were performed in air during 9 days. The results are shown in Fig.14.

Nyquist plots for a 350°C dehydrated RTO sample exposed to air are presented in Fig.14a. The evolution in time can be modeled as an increasing contribution from a Warburg impedance put in series with a parallel of a resistance and a capacitance [28]. This proves that the exposure to air of the 350°C dehydrated sample leads to the emergence of an ionic conduction regime, which becomes predominant as the sample rehydrates.

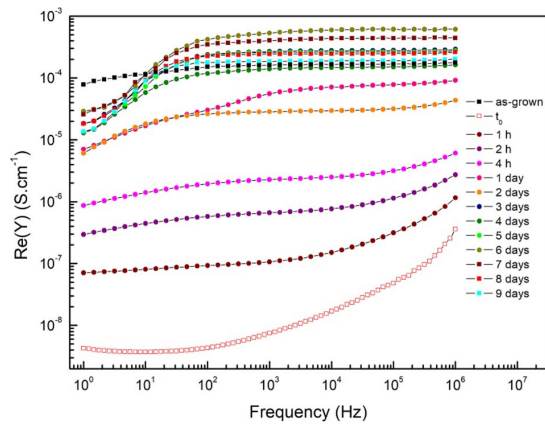
In Fig.14b, the real part of the admittivity is depicted as a function of frequency for different air exposure duration. At high frequency, the observation of a plateau indicates a pure conductivity, which value shows a strong decrease from $1.7 \times 10^{-4} \text{ S}\cdot\text{cm}^{-1}$ at 106 Hz for the as-grown RTO ceramic sample (solid black square on Fig.14b) down to $3.6 \times 10^{-7} \text{ S}\cdot\text{cm}^{-1}$ for the 350°C-dehydrated RTO sample just after exposure to air (open red square on Fig.14b). During the first day of exposure to air, the real part of the admittivity is found to increase rapidly from $3.6 \times 10^{-7} \text{ S}\cdot\text{cm}^{-1}$ to $9.2 \times 10^{-5} \text{ S}\cdot\text{cm}^{-1}$. The magnitude of the real part of the admittivity is still increasing from the third to the sixth day, reaching a maximum value of $6.1 \times 10^{-4} \text{ S}\cdot\text{cm}^{-1}$ and then tends to stabilize around the as-grown value.



(a) Nyquist plot showing the variation of the real and imaginary parts of the complex impedance, from one day to nine days exposure time of a 350°C dehydrated RTO sample to air. [28]

The resulting TGA curve is plotted in Fig.13. A more or less parabolic evolution of the mass of the sample can be observed, which is a signature of a diffusion-limited process. The rapid and significant weight gain confirms the very hygroscopic character of the material.

A strong dependence of the dielectric properties and of the accumulated charge density on the water content has been demonstrated [28]. Dielectric measurements were performed on both as-grown and 350°C-dehydrated RTO ceramic samples. For the latter one, the dielectric measurements were carried out inside a glove



(b) Real part of the admittivity of the 350°C-dehydrated RTO sample inferred from the values of the measured complex impedance. t_0 denotes the time from the beginning of sample exposure to air. [28]

Figure 14: Impact of air exposure duration on the RTO dielectric properties.

3 Internship project

3.1 Exfoliation

Two-dimensional (2D) materials, including for example graphene and transition metal dichalcogenides (TMDs), can be obtained after being successfully cleaved from their layered assemblies into high-quality monolayer samples. Mechanical exfoliation, that was used in the original work to isolate graphene, is one of the most successful techniques to this aim [24]. Because of the lamellar structure evidenced in Figg.4,5, RTO is a potential interesting candidate for exfoliation. An illustration of the process is shown in Fig.15.

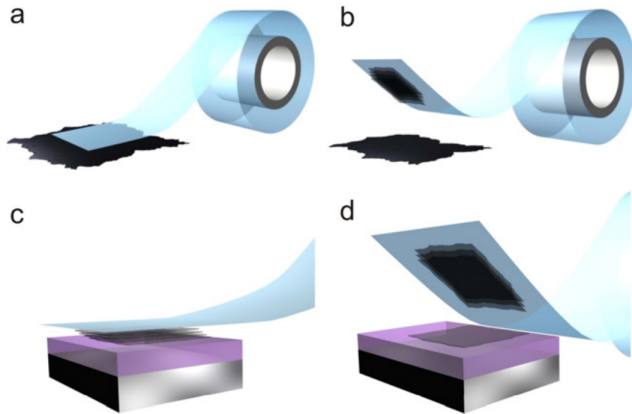


Figure 15: Micro-mechanical exfoliation of 2D crystals. (a) Adhesive tape is pressed against a 2D crystal so that the top few layers are attached to the tape (b). (c) The tape is pressed against a surface of choice. (d) Upon peeling off, the bottom layer is left on the substrate. [23]

The scotch-tape technique was adopted for the micro-mechanical cleavage of the bulk RTO crystals in order to obtain thin crystals. The obtained results have shown that this represents a feasible approach to obtain thin samples although some improvements may be required to fully understand the best conditions for obtaining thinner RTO nanocrystals. For what concerns the substrate, two different materials were considered: a glass substrate, useful for next characterization of the sample and an oxidized Si wafer. In both cases, before the exfoliation, the substrates are cleaned and possibly treated with O_2 plasma to

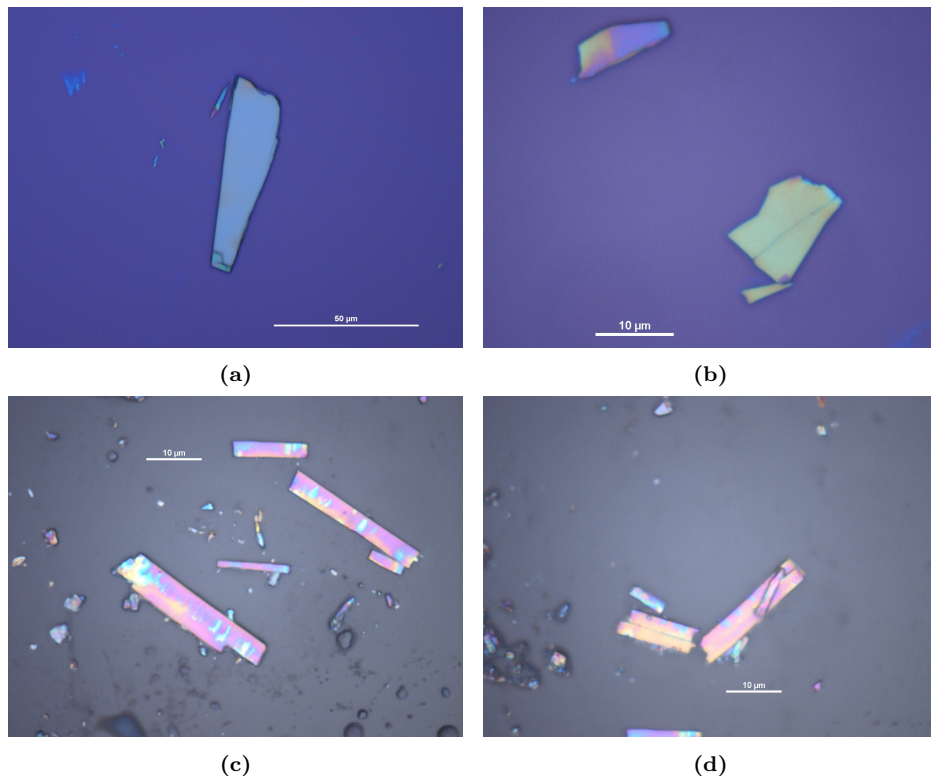


Figure 16: Optical images of exfoliated crystals. (a,b) Si/SiO₂ substrate. (c,d) glass substrate.

make the surface more reactive. This process allows to obtain a cleaner substrate but it has not shown any significant improvement in the quality of the exfoliated material. Fig.16 shows several examples of cleaved samples.

3.1.1 Degradation over time

As demonstrated in section 2.2.4, RTO crystals absorb water from ambient air. This process becomes particularly evident with the exfoliated material. As a matter of fact, the thinner is the crystal the more sensitive to air it is. This aspect is clarified by the samples shown in Fig.17. The rate of deterioration of the samples shows how reactive are RTO crystals when exposed to ambient air. From the optical images it is evident that moisture absorption induces a deformation of the crystal and the formation of fractures possibly leading to the breaking of the same.

If on the one hand water absorption affects the quality of the crystalline structure, on the other it may help in the exfoliation process. What was not understood at the beginning of the project is that bulk crystals pre-exposed to ambient air tends to be easily exfoliated compared to those that are not. This effect may be explained by the intercalation of water molecules which increases the separation between the *ab* planes of the crystal reducing their interaction and helping in the exfoliation process.

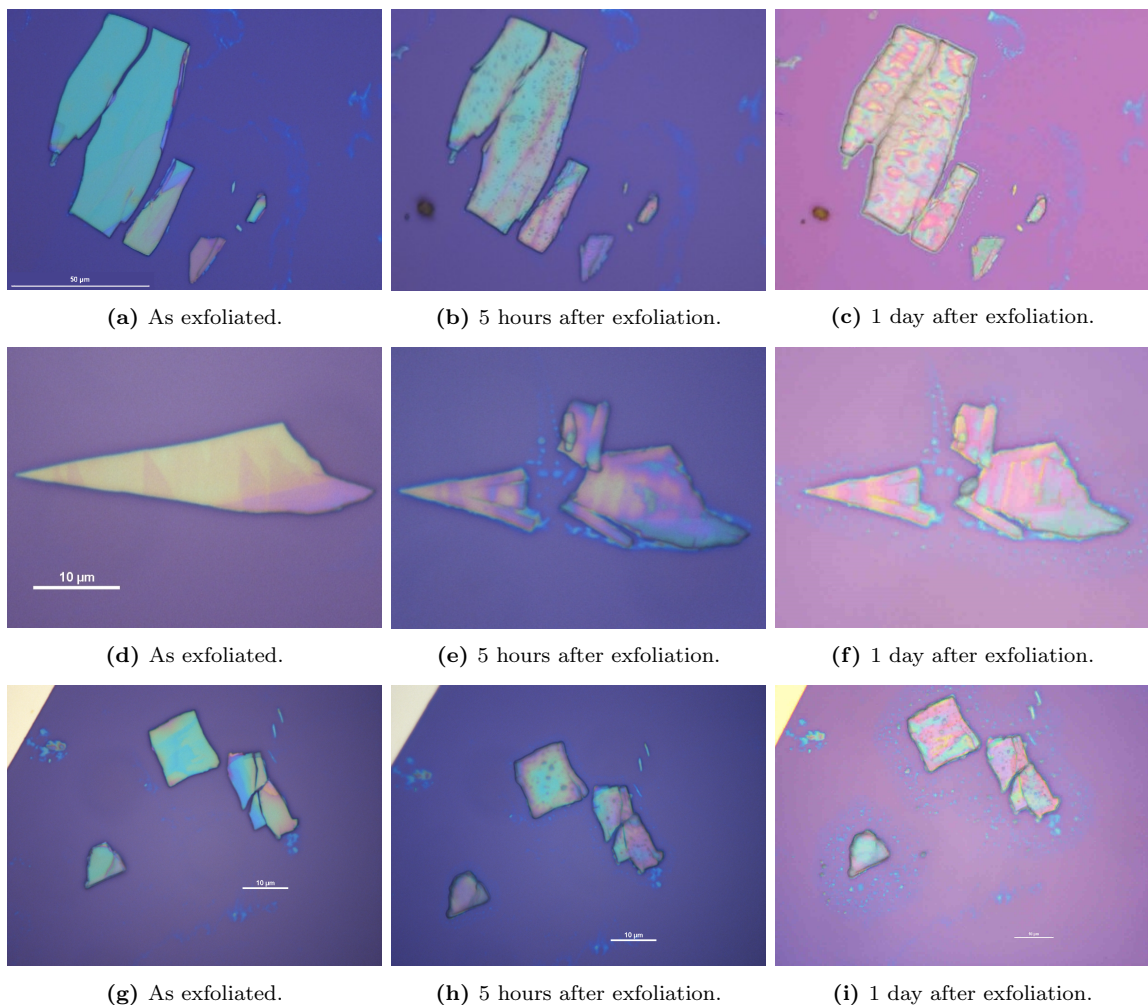


Figure 17: Optical images of exfoliated crystals: degradation with time.

3.2 Characterization: Raman spectroscopy and AFM

3.2.1 Introduction on the techniques

Characterization of RTO nanocrystals is conducted by performing Raman spectroscopy and AFM (Atomic Force Microscope) measurements.

Raman spectroscopy is an optical scattering technique that is widely used for the identification of materials, molecules or crystals, and their characterization. Raman scattering is an inelastic spectroscopy technique, i.e. the incoming monochromatic light undergoes a change in wavelength and is scattered with a different energy. Light can either excite vibrations (phonons) and lose energy or pick up energy from present thermally excited vibrations (see Fig.18). In the former case, the mechanism is referred to as Stokes Raman scattering, in the latter as Anti-Stokes Raman scattering. The energy shift is mostly dependent on the material composition and structure and not the wavelength of the excitation light. Therefore, Raman spectroscopy measures the energy shift of the Raman scattered light relative to the incident one, which is characteristic to the sample that is being investigated. Raman scattering is named after Chandrasekhara Venkata Raman and was discovered in 1928 by Raman and Kariamanikkam Srinivasa Krishnan [11].

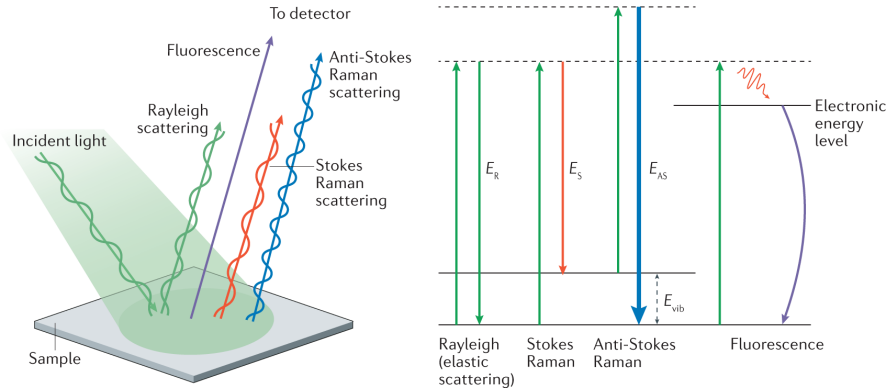


Figure 18: Principle of Raman scattering: (Rayleigh) no phonon is involved; (Stokes) A phonon is created, part of the energy is lost; (Anti-Stokes) A phonon is annihilated, energy is gained by the re-emitted photon. If no electronic energy level is available fluorescence is absent. [10]

Atomic force microscopy is a high-resolution non-optical imaging technique first demonstrated by Binnig, Quate and Gerber in 1985 [7]. It belongs to the class of Scanning Probe Microscopy (SPM) techniques which exploit a physical probe to image the surface of a specimen by scanning the same. The nature of an SPM probe tip depends entirely on the type of SPM being used or, in other words, on the physical quantity to be probed.

The basic operation principle of a standard AFM system with optical feedback [8] (Fig.19) involves scanning an AFM probe with a sharp AFM tip over a sample surface in a raster pattern. The AFM tip is integrated near the free end of a flexible cantilever. As the AFM tip moves over features of different height the deflection of the AFM cantilever changes. This deflection is tracked by a laser beam reflected from the back side of the AFM cantilever and directed into a position sensitive photodetector.

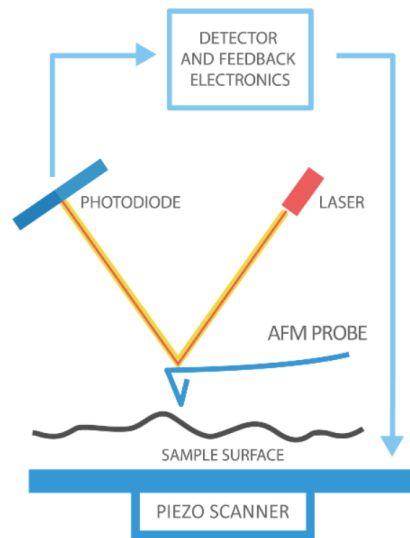


Figure 19: AFM schematic. [9]

3.2.2 Setup: technical information

AFM and Raman measurements were carried out with a Witec-alpha300RA microscope equipped with a 532 nm laser excitation source coupled to a Witec-UHTS300 micro-Raman spectrometer.

For the Raman spectroscopy of nanocrystals, a 100x objective was used with a laser power of 5 mW or 10 mW. Each Raman spectrum is an average of ten different Raman spectra acquired in a row and the spectral resolution is $\approx 4 \text{ cm}^{-1}$, when using a 600 g/mm grating monochromator (in the following G1 grating), or $\approx 1 \text{ cm}^{-1}$, when using a 1800 g/mm grating monochromator (in the following G2 grating). If not specified, measurements are performed with the G1 grating equipped.

3.2.3 Atomic force microscope measurements

AFM measurements were conducted in order to establish the typical size of the RTO nanocrystals that can be achieved by performing a micro-mechanical exfoliation by scotch-tape technique. As a matter of fact, this method may result not appropriate to obtain samples that are few nanometers or few tenths of nanometers thick. It is important, in this sense, to assess the limits of the scotch-tape technique and to understand if other exfoliation processes, for example relying on chemistry, should be investigated.

For measuring RTO nanocrystals thickness, AFM was used in acoustic (AC) mode, also known as tapping mode. In this detection scheme, the cantilever is driven at a constant frequency near resonance, and force gradients are detected as variations in the amplitude or phase of of the mechanical vibration of a cantilever. A raster scan of the tip over the surface in this mode provides an image of the force gradient variations above the surface which, through the van der Waals interaction, can be interpreted as an image of the surface profile [25].

Overall, 74 samples have been analysed and a trivial statistics of their thicknesses is shown in Fig20. The exfoliated RTO crystals have been categorized in 20 bins from 50 nm to 1000 nm centered around multiples of 50 nm. Each bin collects nanocrystals with thickness in an interval of 50 nm around its center.

A further qualitative distinction, as highlighted in the histogram, concerns samples with

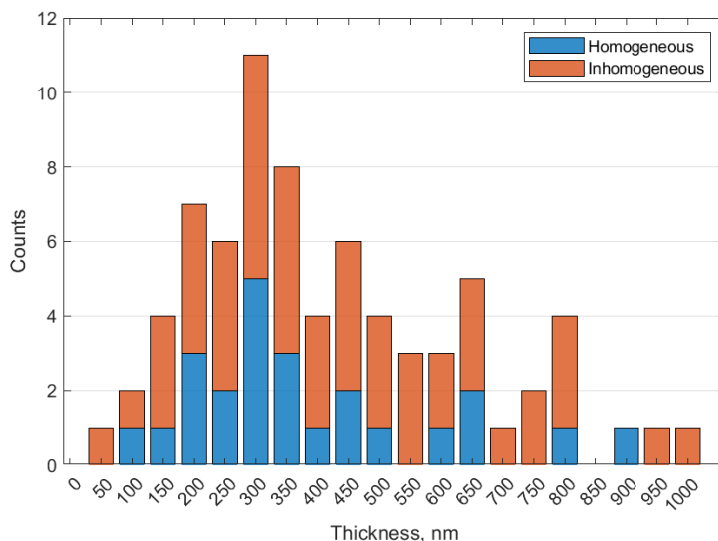


Figure 20: RTO nanocrystals arranged in 20 bins as a function of their thickness. Each bin is centered around a multiple of 50 nm with radius of 25 nm. A distinction between samples with homogeneous or inhomogeneous surfaces is made.

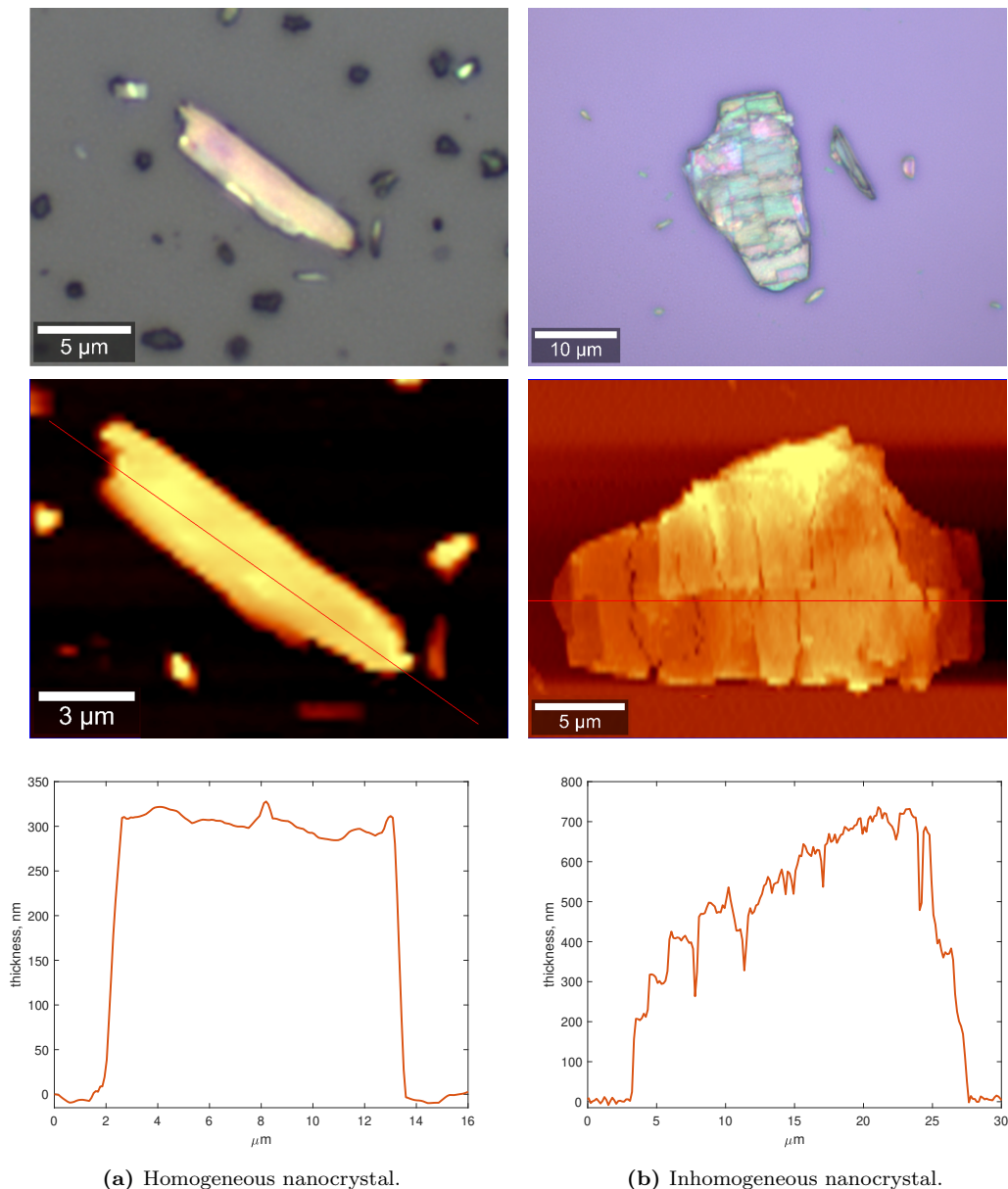


Figure 21: Exfoliated RTO crystals: example of different surface topographies. From top to bottom: optical image, AFM image, profile extracted from the AFM measurement along the red line shown above.

a homogeneous surface and samples with an inhomogeneous surface. As an example, two samples with the corresponding AFM images are shown in Fig.21.

As illustrated in Fig.20, most of the samples are in the range between 150 nm and 450 nm and typically they do not have a homogeneous surface but some irregularities and steps are present.

For what concerns the limits of the scotch-tape exfoliation, I have reasons to believe that by mastering the technique, thinner RTO nanocrystals could be feasibly obtained. This possibility is suggested by the fact that the majority of the samples belonging to the left region of Fig.20 have been analysed two months after the beginning of the project.

3.2.4 Raman spectroscopy measurements

RTO nanocrystals have been studied through micro-Raman spectroscopy in order to investigate possible local structure changes from bulk crystals to thin sam-

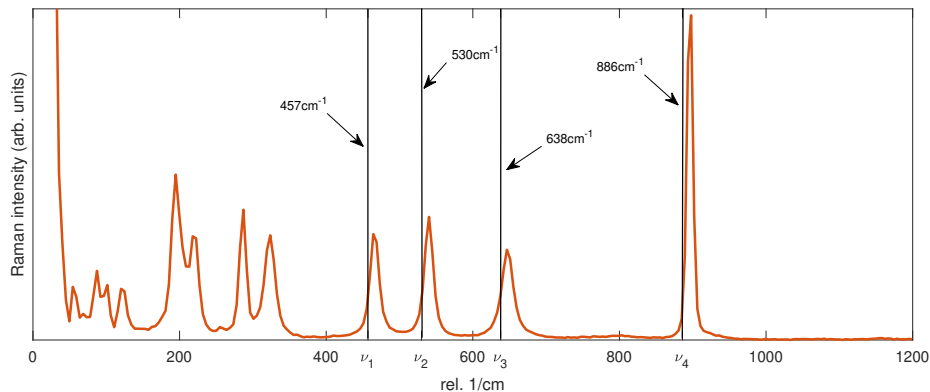


Figure 22: Raman spectrum of as-grown $\text{Rb}_2\text{Ti}_2\text{O}_5$ crystal

ples. Only Stokes Raman signal has been collected and analysed. The starting point was to measure the Raman spectrum of bulk RTO, shown in Fig.22.



Figure 23: Optical image of an exfoliated crystal.

The four phonon modes in the high-frequency part of the spectrum (above 400 cm^{-1}), ν_1 , ν_2 , ν_3 and ν_4 , are compared to the experimental values obtained in [21] and shown in Fig.8: respectively 457 cm^{-1} , 530 cm^{-1} , 638 cm^{-1} and 886 cm^{-1} . What is observed is a shift of $\approx 10\text{ cm}^{-1}$, which is common to all the peaks. The values extracted from Fig.22 are 466 cm^{-1} , 540 cm^{-1} , 647 cm^{-1} and 897 cm^{-1} . The spectrum in Fig.22 is considered as a reference to identify possible changes in the spectra of RTO nanocrystals.

A typical Raman spectrum of an exfoliated crystal is shown in Fig.24, corresponding to the sample presented in Fig.23. It is evident from this Raman measurement that the peak corresponding to the ν_4 phonon mode is suppressed, whereas the remaining phonon modes of interest, ν_1 , ν_2 and ν_3 are shifted. In particular, ν_1 undergoes a redshift whilst the ν_2 and ν_3 phonon modes are blueshifted. Moreover,

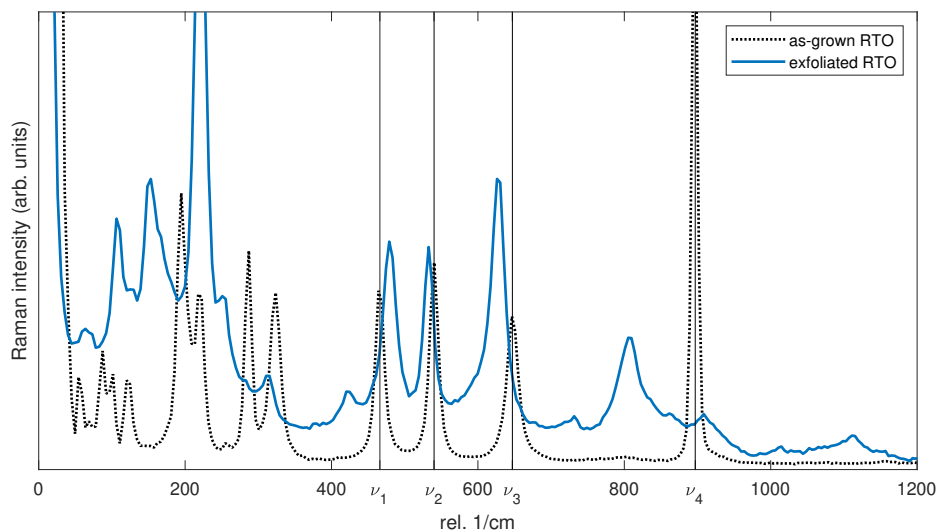


Figure 24: Raman spectrum of the sample in Fig.23. The values of ν_1 , ν_2 , ν_3 and ν_4 (listed in the text) are taken from the peak values of the reference spectrum of Fig.22, here represented by the dotted line.

some additional peaks arise.

The same trend was already observed in previous measurements [21]. In Fig.25, Raman spectroscopies measurements of an as-grown $\text{Rb}_2\text{Ti}_2\text{O}_5$ crystal and of an 'activated' crystal are reported [21].

An activated crystal is a sample that underwent an activation process consisting, as described in [3], in an annealing process at 400 K under He atmosphere lasting a couple of hours. The activation process was thought to be responsible for a strong enhancement of the electrical properties of RTO, as a drop in the resistivity of at least 4 orders of magnitude was seen in treated samples.

Activated crystals were also showing an energy shift of some phonon modes and the emergence of additional peaks. The same features are observed in RTO nanocrystals which are just exfoliated from as-grown crystals but without any additional process. This points toward the role of water absorption as one possible cause of the changes in the local structure of RTO and consequently on its Raman activity.

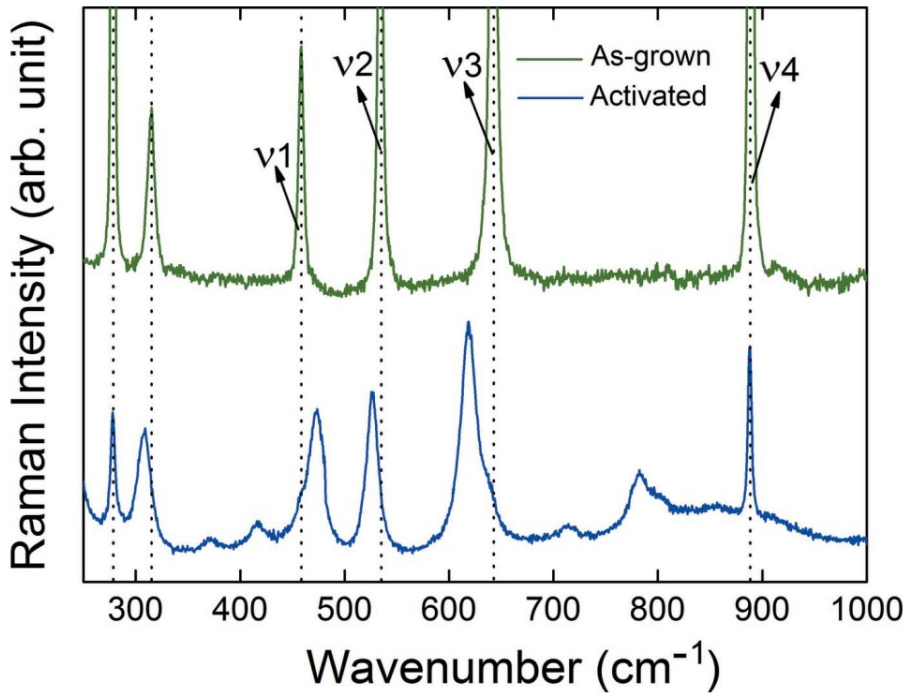


Figure 25: Raman spectra taken at 300 K for an as-grown sample (green line) and for an activated sample (blue line). Note the energy shift produced by the activation process for the ν_1 , ν_2 , ν_3 phonon modes whereas 4 remains unaffected. Additional peaks are also produced by the activation. [21]

3.2.5 Raman spectra size-dependence

AFM and Raman measurements were conducted in combination to investigate possible size-dependent modification in the Raman activity of RTO nanocrystals. No evidence of such dependence was seen. Raman spectra collected from distinct samples were different but no correlation with the nanocrystals size was identified.

In Fig.26 is reported, as example, the comparison between two 300nm-thick exfoliated RTO samples. In particular, the optical images are shown, together with the AFM ones, the flakes profile extracted from the latter and finally the Raman spectra. The two curves differ both in terms of the Raman peaks intensity and position, and also additional peaks, which are not found in the blue spectrum, are present in the orange curve. In particular, the ν_1 , ν_2 , ν_3 phonon modes are visible in the latter, making it more similar to the bulk

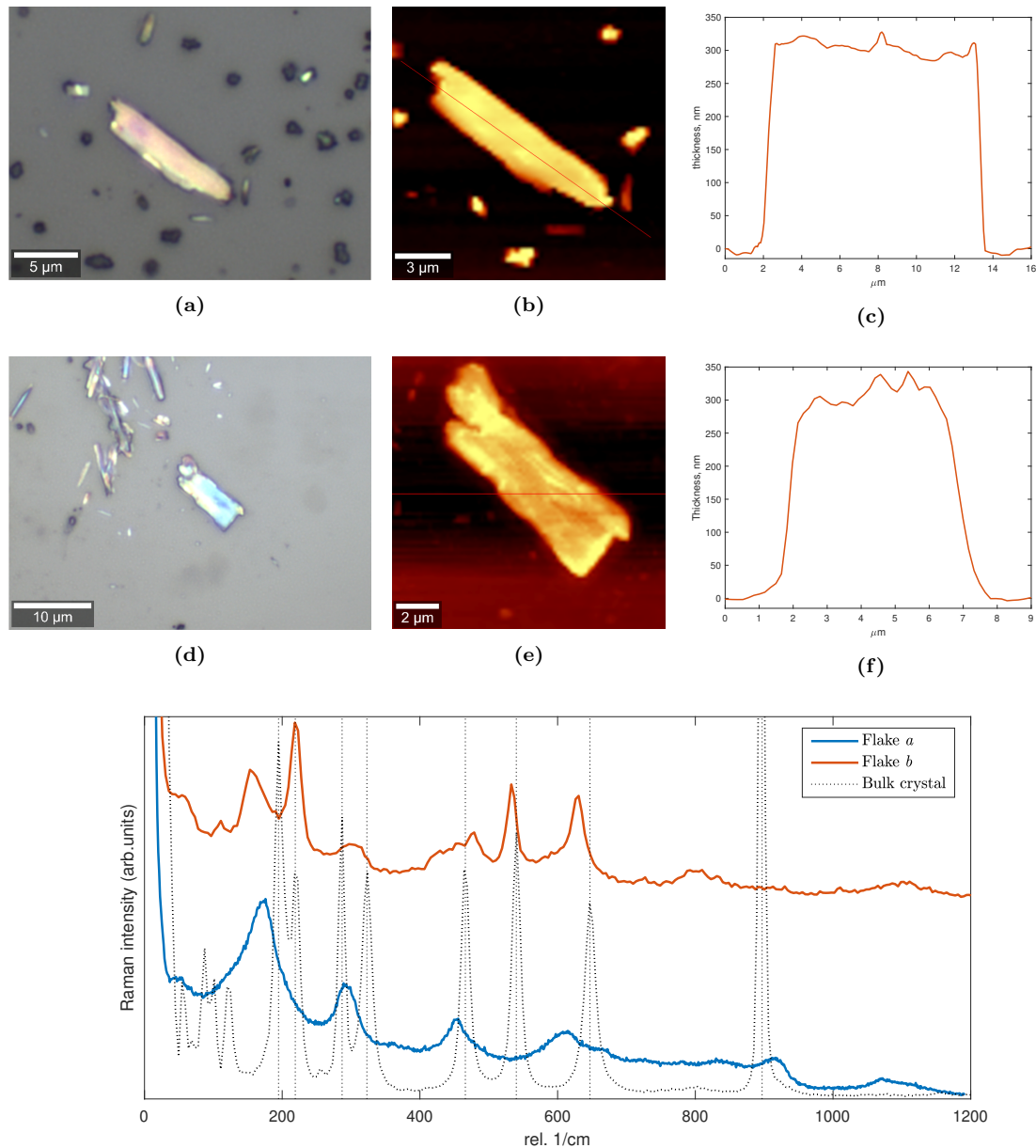


Figure 26: (a,b,c) Flake *a*: respectively optical image, AFM image and extracted profile along the red line. (d,e,f) Flake *b*: respectively optical image, AFM image and extracted profile along the red line. (Bottom) Comparison of the Raman spectra of two 300nm-thick nanocrystals. The blue curve is measured with the G2 grating monochromator, the orange one with the G1 grating monochromator. The curves are displaced for clarity. The spectrum of the bulk crystal is also present as reference.

crystal spectrum, whereas the ν_2 peak is not detected in flake *b* (Fig.26d).

As a general rule, two different samples with the same thickness typically have different Raman spectra. At the same time, Raman spectra extracted from the same nanocrystal share exactly the same features regardless of the RTO thickness.

To show this, let us consider the samples shown in Fig.27,28,29. The thickest (Fig.27) and the thinnest (Fig.29) share a step-terrace structure and are suitable for analysing Raman spectra collected from regions with different thickness, but belonging to the same nanocrystal. The third sample (Fig.28) has an intermediate size.

Fig.30 compares the Raman spectra obtained from these samples. The local thickness of the RTO nanocrystal where each spectrum is measured, is indicated in the legend. The signal intensity drops together with the size of the flakes as the bottom curves are noisier

than the top ones. Apart from this, there is no spectrum exhibiting distinctive features. The emergence of a peak around 1100 cm^{-1} occurs in the thinnest sample, but it corresponds to the increasing signal coming from the glass substrate due to the progressively reduced amount of RTO on top of the same.

Fig.30 confirms that Raman spectra do not show a particular size-dependence, but generally, they share common characteristics if collected from the same sample, even from regions with different thickness. As a proof, the three top spectra in the figure, measured on the RTO in Fig.27, are equal, as well as the three bottom ones, measured on the RTO in Fig.29.

These finding point towards the level of hydration and/or disorder as main factor dictating the Raman activity, prevailing on the thickness influence.

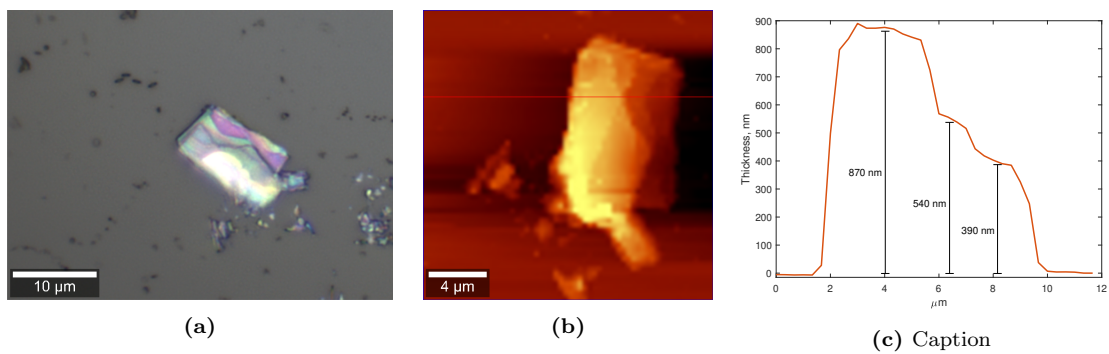


Figure 27: Thick sample: (a) optical image of the nanocrystal, (b) AFM image of the nanocrystal, (c) profile along the red line extracted from the AFM measurement.

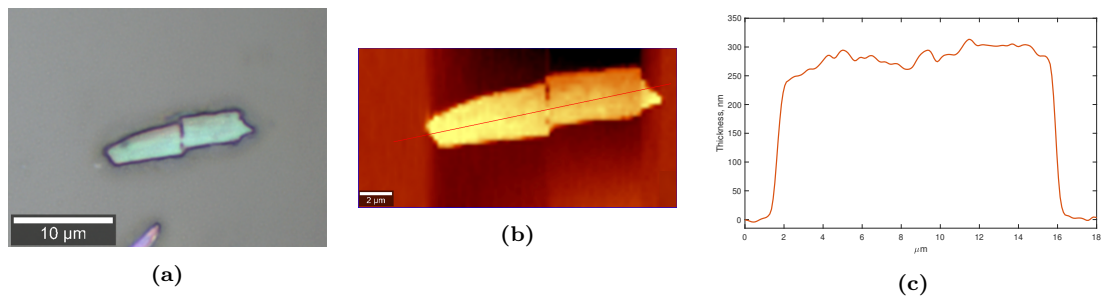


Figure 28: Intermediate sample: (a) optical image of the nanocrystal, (b) AFM image of the nanocrystal, (c) profile along the red line extracted from the AFM measurement.

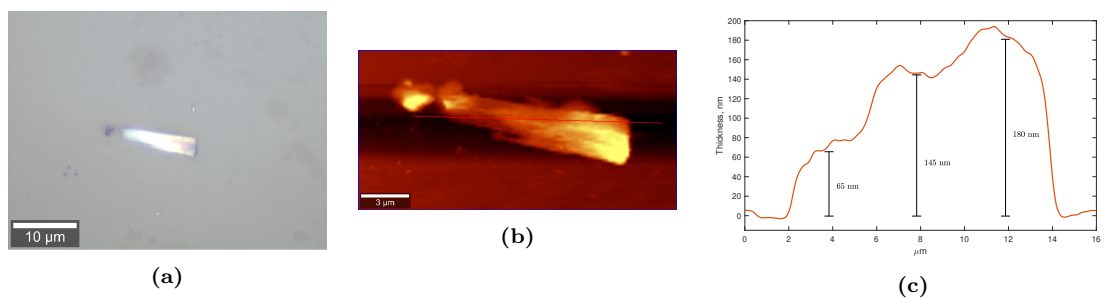


Figure 29: Thin sample: (a) optical image of the nanocrystal, (b) AFM image of the nanocrystal, (c) profile along the red line extracted from the AFM measurement.

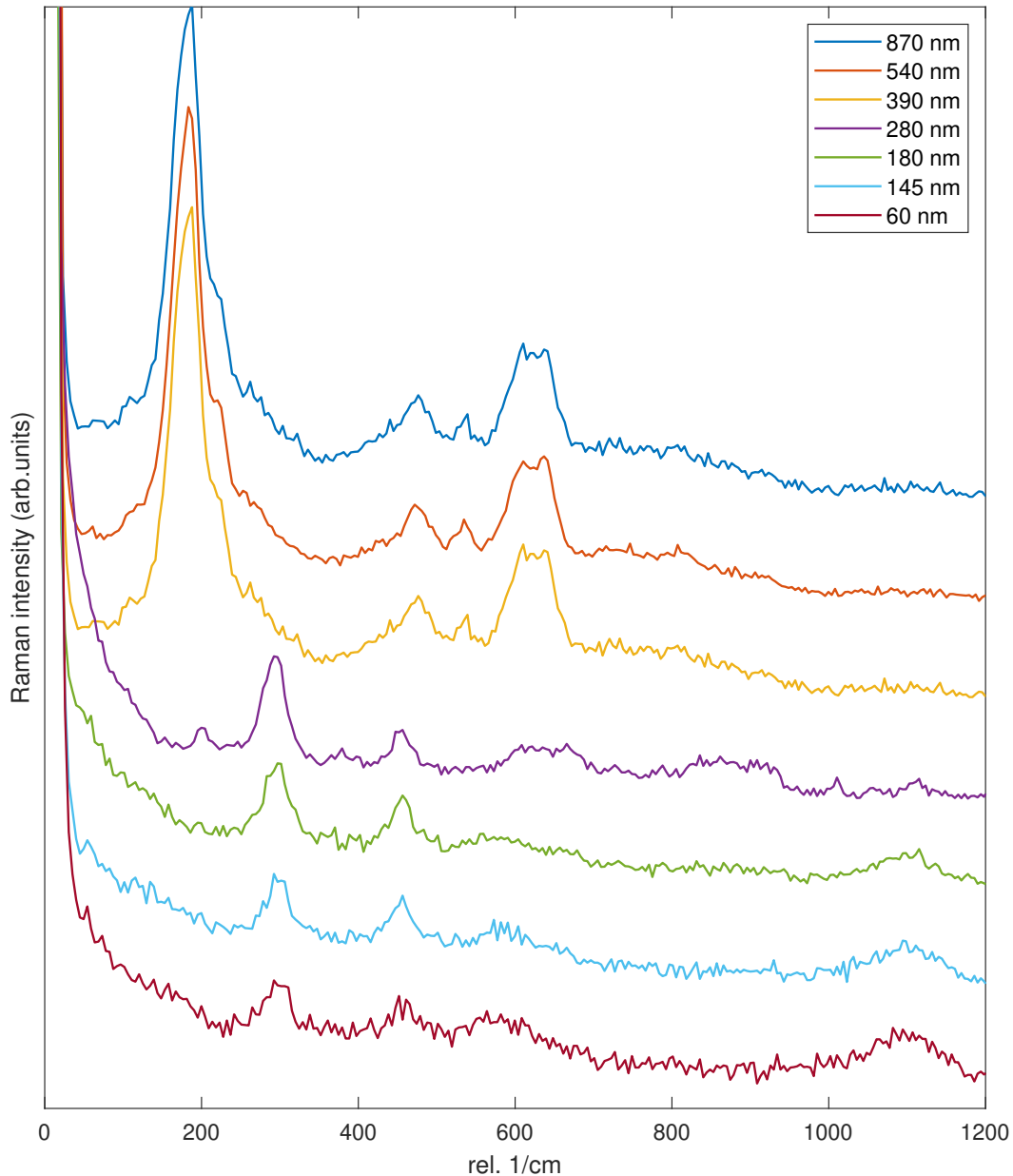


Figure 30: Comparison of the Raman spectra collected by the samples illustrated in Fig.27,28,29. The curves are displaced for clarity. The three top curves are collected from the flake in Fig.27. The three bottom ones from the sample in Fig.29. Note that spectra obtained from the same nanocrystal are almost identical.

3.3 Device fabrication

The device fabrication consists in realizing electrical connections at the edge of RTO nanocrystals in order to subsequently perform electrical transport measurements. It is entirely carried out in cleanroom. Micro- and nanofabrication techniques employed include photo- and e-beam lithography, e-beam evaporation, lift-off. Also the “hot pick-up” transfer method, typically used for assembling van der Waals heterostructure starting from 2D material flakes, is implemented.

3.3.1 Introduction on the techniques

Photo- and e-beam lithography

Photolithography, or UV lithography, is a patterning process used in microfabrication. It uses light to transfer a geometric pattern from an optical mask to a photosensitive, i.e. light-sensitive, photoresist on the substrate. Electron beam lithography (EBL) is an analogous process differing from the previous by the radiation, namely an electron beam, used to expose the resist. A series of chemical treatments then, either etches the exposure pattern into the material or enables deposition of a new material in the desired pattern upon the material underneath the photoresist.

In this work, the resist used for the photolithography is AZ 5214E. It is an image reversal photoresist suitable for lift-off techniques because of the negative side wall profile obtained after the development. The photolithographic process starts with the spin-coating of the resist onto the substrate and a bake at 110°C for 1 minute. A first exposure is then performed through a photolithographic mask, in hard contact with the sample, corresponding to the negative image of the final pattern to be reproduced. The exposed parts of the resist become more soluble. Successively, the sample is baked at 120°C for 2 minutes. This step is called reversal bake and causes the polarity switching by cross-linking the previously exposed resist. At this stage the resist is not ready for the development, but a flood exposure is required. The whole sample is shined and the resist that in the first exposure remained dark, now becomes more soluble than the rest which was cross-linked with the baking. Finally, the development is done by immersing the sample in a developing solution, AZ 326 MIF or AZ 400K in this case, and by rinsing with water. At this moment, the pattern is already reproduced on the sample, which it is ready for the metal deposition.

The process for the e-beam lithography is slightly different. The resist used is a positive one, namely a PMMA (polymethyl methacrylate)/Anisole 2:1 solution. After the spin-coating of the substrate, the sample is baked at 180°C for 1 minute and the EBL is performed with a Zeiss scanning electron microscope (SEM). After the exposure, the development is done in a MIBK (Methyl Isobutyl Ketone)/Isopropanol 3:1 solution.

E-beam evaporation

Evaporation is a physical vapor deposition (PVD) technique, used mostly for metal layers and alloys, enabling thin film growth achieved by the accumulation (condensation) of a vapor onto a cooler substrate. In e-beam evaporation a filament is heated up to electrons emission, which are accelerated and deviated to hit the material to be deposited, hosted in a crucible. The material is heated up and the evaporation occurs, followed by the deposition onto the substrate which is placed upside down above the crucible.

The metals deposited for the realisation of the final device are titanium (Ti) and gold (Au). The latter is responsible for the actual electrical connection while titanium is just used as adhesion layer. In fact, gold may not adhere well to the substrate and may be removed during lift-off, which represents the last fabrication step. It is performed to remove the remaining resist and the unwanted metal deposited on top of it, to release the final device. Lift-off consists in leaving the sample in acetone for indicatively more than 3 hours (there is no specific duration) and rinsing it with isopropanol.

Hot pick-up

In order to transfer the exfoliated materials the hot pick-up transfer technique is used. To perform the pick-up and the drop-down of the nanocrystals, the temperature of a polypropylene carbonate (PPC) coated polydimethylsiloxane (PDMS) drop, produced on a glass slide, is increased above the PPC glass transition temperature ($\approx 40^\circ\text{C}$). The process is carried out in cleanroom by using two independent micro-manipulators,

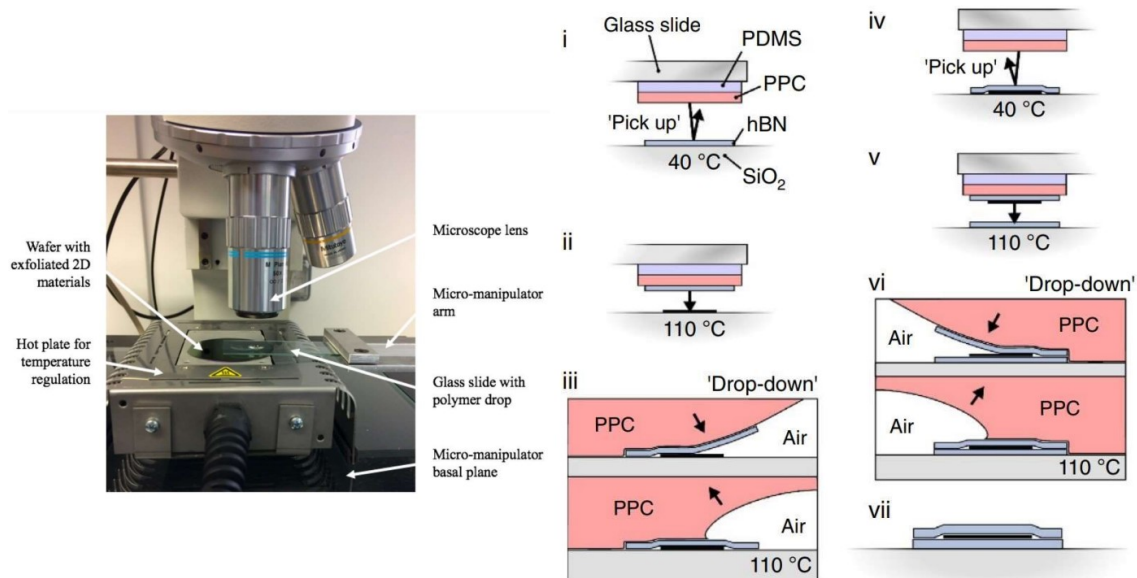


Figure 31: (Left) Set-up for hot pick-up transfer: a hot plate is used to modulate the temperature; the wafer substrate containing the exfoliated 2D samples is fixed on the hot plate and an optical microscope is used to locate the flakes by optical contrast; a second micro-manipulator moves the glass-supported PDMS/PPC drop. [26]

(Right) Schematic process flow for assembly of 2D heterostructures by pick-up and drop-down. In this specific case, the assembly of a graphene/hBN heterostructure is illustrated. [27]

one for the substrate and one for the drop, and an optical microscope. The set-up and a schematic of the process are shown in Fig.31. For the pick-up, the temperature is set in the range between 65°C and 75°C , the exfoliated flake is contacted with the drop and pulled up from the substrate. For lower temperatures the PPC drop would remain glued on the substrate, while for higher temperatures it would delaminate from the PDMS. The drop, together with the flake is then approached to another substrate for the drop-down step. In this step, after the contact with the substrate, the pulling-up of the drop has to be as slow as possible. In this way, the interaction between the flake and the substrate dominates and the flake will leave the polymer drop. If the adhesion of the flake with the substrate is poor, the temperature can be increased to 95°C so as to melt the PPC coating that will remain on the substrate. Finally, an acetone/isopropanol cleaning is recommended to eliminate polymer residues.

3.3.2 Design of the device

As a first approach, the aim was to realise the simplest possible design to electrically connect the RTO nanocrystals and perform the measurements. To date, two possibilities have been explored. The first consists in exfoliating RTO on an oxidized Si wafer and subsequently perform photolithography and e-beam evaporation to pattern and deposit gold contacts at the edge of the nanocrystals. The second requires the hot pick-up method as additional step. In fact, it consists in pre-patterning and depositing Au contacts on a Si/SiO₂ wafer and then to transfer exfoliated RTO on top of them to obtain an electrically connected sample.

Although the first process seems the simplest to be implemented, just one over more than 40 samples that were actually prepared, survived the development of the resist and was ready for the metal deposition. It took several weeks to figure out the causes of the poor yield of this process. The main problem has been determined to be the high reactivity

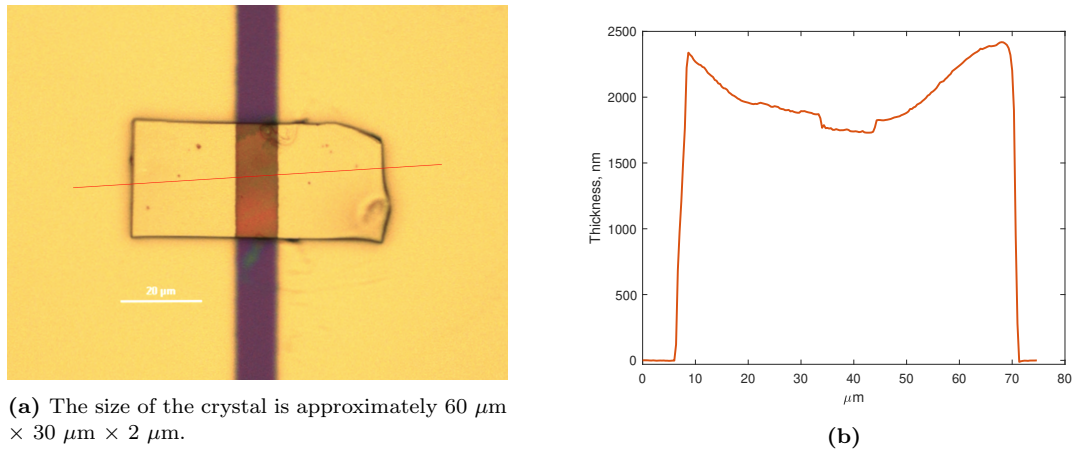


Figure 32: First RTO device. (a) Optical image after metal deposition. (b) Profile extracted from AFM measurements.

of RTO to water.

The problem is not represented by UV lithography itself. Rather, the critical aspect is the presence of water in the solutions used in the process. If RTO deteriorates at air by just absorbing moisture, the degradation when immersed in liquid water is even worse and faster. The crystal behaves as a sponge and is distorted, reducing also the adhesion to the substrate. This explains why, after performing the development of the resist, in most of the cases, the RTO nanocrystals detached from the substrate and the resist was well developed everywhere but on the area occupied by RTO. In many instances, samples were rinsed with water. This step can simply be avoided by cleaning with isopropanol, but does not solve the problem. In fact, both the developers of the AZ 5214E resist contain water. The AZ 326 MIF is actually a solution of 2.38% TMAH (TetraMethylAmmonium Hydroxide) in H_2O . The AZ 400K is based on buffered KOH and, for developing, it is 1:4 diluted in H_2O (1 part of concentrate and 4 parts of deionised water). For this design, just photolithography has been done, whereas EBL has not yet been attempted.

The only sample that was obtained probably survived the development because of its remarkably high average thickness of $\approx 2 \mu\text{m}$, as confirmed by successive AFM measurement. After the deposition of 5 nm of Ti and 100 nm of Au, the sample looked as shown in Fig.32a. Because of the huge discrepancy between the metallic layer thickness and

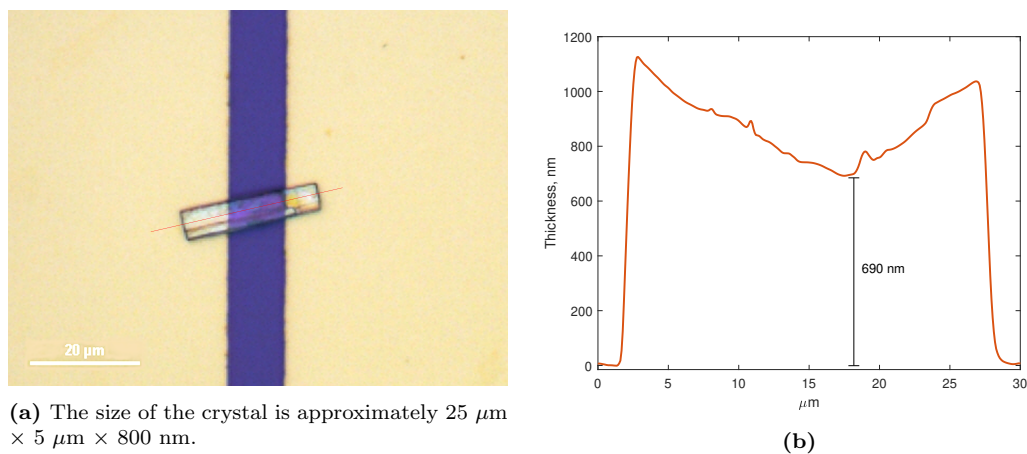


Figure 33: Second RTO device. (a) Optical image after metal deposition. (b) Profile extracted from AFM measurements.

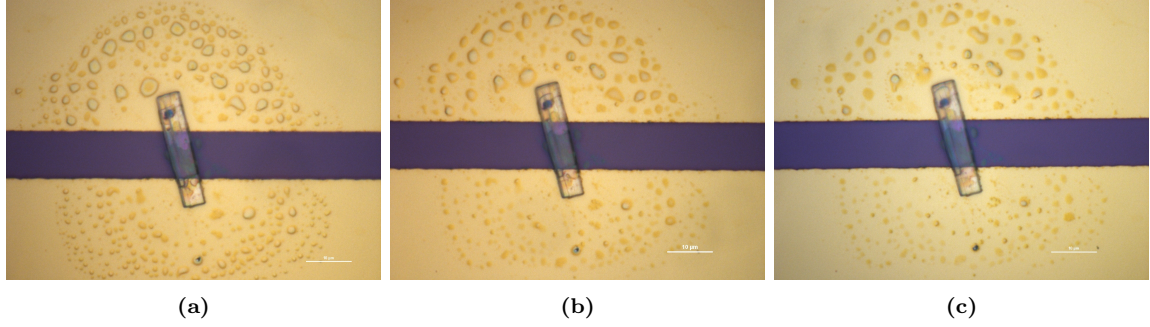


Figure 34: Dehydration of the sample in Fig.33. (a) Out of the vacuum chamber after 15 hours. (b) After dehydration bake at 120°C for 4 minutes. (c) After successive dehydration bake at 120°C for 10 more minutes.

that of RTO (unknown before the deposition), electrical contact between the two was not properly established. As a consequence, any electrical measurement attempt was vain.

I believe this device structure can guarantee a better quality of the electrical connection at the RTO-metal interface, compared to the one where the crystal is simply positioned on top of the Au contacts, after their deposition. For this reason, it may be of interest to perform EBL, to avoid the presence of water in the process and try to increase the device yield for this configuration.

Three different devices were realised following the second design. In particular, for one of them, electrical measurements have been conducted and some $I - V$ characteristics have been measured (see following section). The device and its profile are shown in Fig.33. To avoid any degradation with time, the sample was put under high vacuum. When removed from the chamber, approximately after 15 hours, the sample looked as in Fig.34a, where the presence of droplets all around the RTO flake is highlighted. A plausible explanation may be that the nanocrystal had already absorbed a significant amount of water that was partially or totally released when put in vacuum. Optical images of the sample have also been taken after a dehydration bake at 120°C for 4 minutes (Fig.34b), and after a second one, always at 120°C for 10 more minutes (Fig.34c). This process visibly affects the number and the size of the droplets.

3.4 Electrical measurements: preliminary results

3.4.1 Measurement set-up

Electrical measurements performed on the sample in Fig.33a, after rehydration of the flake, allowed to obtain some preliminary result. $I - V$ curves have been obtained by generating extremely slow ramps (≈ 10 minutes per ramp) of voltage by means of a Yokogawa 7651 programmable DC source. A DLPCA-200 low noise current amplifier was used to measure very low currents, of the order of fractions of nA. The output voltage of the amplifier was read using an Agilent 34401A digital multimeter.

3.5 $I - V$ measurements

Considering previous measurements conducted on RTO bulk crystals [3] (see Fig.9), the applied voltages ranged from -20 V to +20 V with typical distances of $\approx 1000 \mu\text{m}$ between the contacts, implying a maximum applied electric field $\mathcal{E}_{\text{max}} \approx 20 \text{ kV/m}$.

As a first approach to perform the measurements on the nanocrystal in Fig.33a, I tried to keep an equivalent applied electric field. Surprisingly, the system did not show any significant response until the voltage range was extended to almost the same values as in

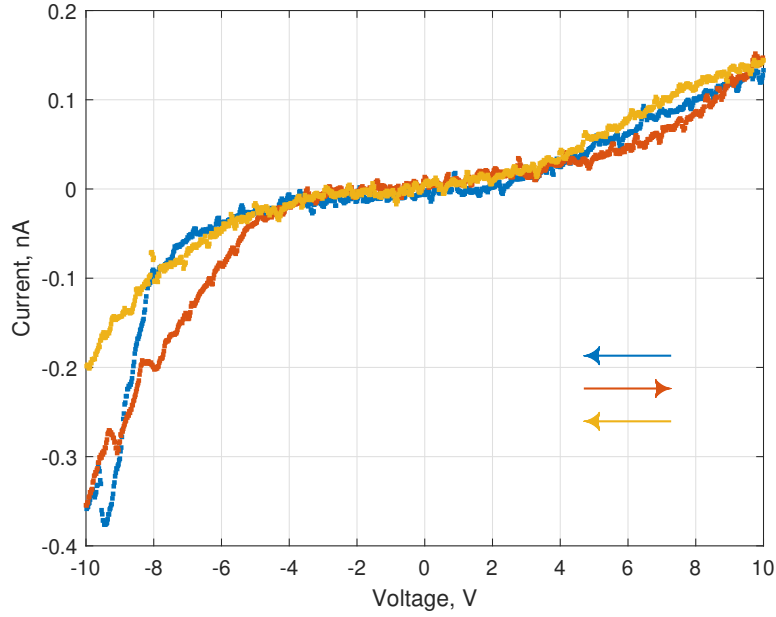


Figure 35: Current versus applied voltage for the sample in Fig.33a. The voltage step is 0.02 V and the time step is 1 second. One measurement lasts more than 15 minutes.

[3]. Being the gap between the electrodes equal to 10 μm , the maximum applied electric field reached values $\sim 1 \text{ MV/m}$.

In Fig.35, some $I - V$ measurements are shown. The voltage sweep direction is indicated by the arrows. The curves have been taken consecutively, with no pause between each other. The voltage step was set to 0.02 V and the step time to 1 second. Differential conductance values have been estimated from the graph. The maximum value has been extracted from the left region of the blue curve and corresponds to $\approx 2 \times 10^{-10} \text{ S}$. For the other curves, always for negative voltages, the maximum values are $\approx 5 \times 10^{-11} \text{ S}$. Close to the center of the characteristic, the conductance drops to $\sim 1 \times 10^{-12} \text{ S}$. Taking into account the size of the sample, the maximum estimated conductivity is $\sigma \approx 5 \times 10^{-6} \text{ S}\cdot\text{cm}^{-1}$, corresponding to a resistivity $\rho \approx 2 \times 10^5 \Omega\cdot\text{cm}$. These values are in agreement with the expectations based on previous results [3,28]. As stated in section 2.2.2, typical values of resistivity for as-grown (non-activated) samples are above $1 \times 10^8 \Omega\cdot\text{cm}$, but a drop of at least 4 orders of magnitude is observed in activated crystals. My result is a confirmation that the RTO activation is mainly determined by the hydration level of the crystal and that the annealing process is not a determining factor for the conduction enhancement, as reported in [3].

These are just preliminary results. As a matter of fact, the characteristic shown in Fig.35 does not correspond to the reference one (Fig.9). There is no clearly observable hysteresis and the current drop at the edges of the characteristic is absent.

The reasons for this behaviour are unknown. Initially, the measurement duration was thought to be not long enough to observe the aforementioned drop. This hypothesis has not been confirmed, rather it became less convincing. In fact, after leaving the sample biased with high voltage (fixed) for long time, the current started to increase rather than decreasing, sometimes extremely rapidly.

This is proved by Fig.36,37,38. The measurements have been performed in three different days. In Fig.36, the first three curves were obtained consecutively, but before

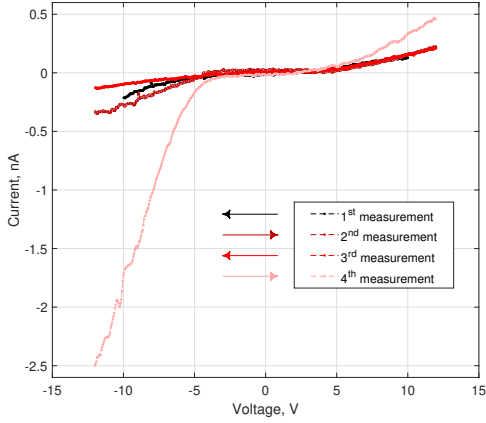


Figure 36: Current vs applied voltage measurements. Voltage ramps are obtained with voltage steps of 0.02 V with 1 second of time step. Arrows show the sweep direction for each curve. Note the rise, in absolute value, of the current for the delayed measurement (curve 4).

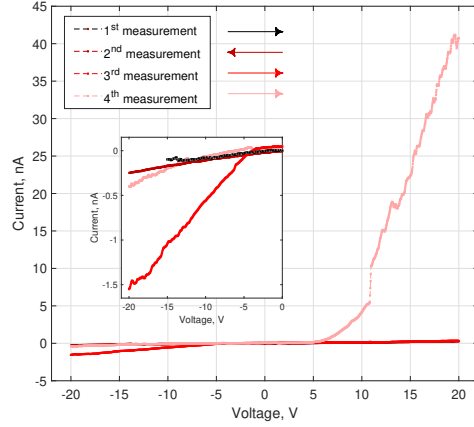


Figure 37: Current vs applied voltage measurements. Voltage ramps are obtained with voltage steps of 0.05 V (curves 1,2,3) and 0.025 V (curve 4) with 1 second of time step. Arrows show the sweep direction for each curve. (Inset): characteristic for negative applied voltages.

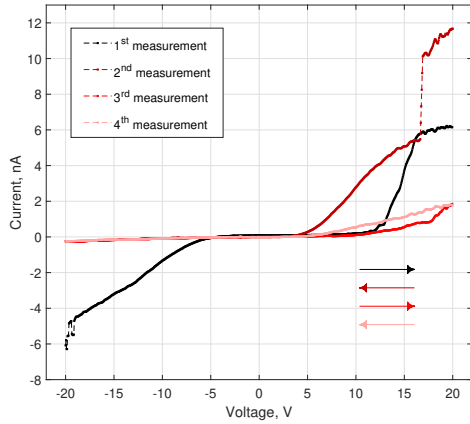


Figure 38: Current vs applied voltage measurements. Voltage ramps are obtained with voltage steps of 0.05 V with 1 second of time step. Arrows show the sweep direction for each curve. Note how the characteristic starts resembling again the ones shown in Fig.35 and the first ones of Figg.36,37.

the fourth one started, the sample was left at -12 V for more than 1 hour. The absolute value of the current increased from 0.13 nA (3rd curve) up to 2.5 nA, and also the current measured at the end of the ramp was higher than the previous ones. Of the four curves presented in Fig.37, the first two were obtained consecutively, the third one after approximately 20 minutes at fixed voltage equal to -20 V, and the fourth after 1 hour and a half at +20 V. Again, jumps in the current at the edges of the curves can be seen. Surprisingly, this process does not seem to alter the behavior of the device since, as shown in the left part of the fourth measurement (see inset of Fig.37), the curve seems to recover the original behavior.

This is also observed in Fig.38, where the presented measurements were taken consecutively one with respect to the other after

the sample was left more than 5 hours at -20 V. Apart from some abrupt jump of the current, the sample seems to recover its original behavior, with currents of the order of fraction of nA.

Up to now, there is no sufficient information to interpret these outcomes. Further electrical measurements on more samples, possibly with different design, are needed to validate or discard these findings.

4 Conclusions

4.1 Overview

The already established and well known scotch-tape technique for micro-mechanical exfoliation has been investigated as possible process to obtain nanometrically thin $\text{Rb}_2\text{Ti}_2\text{O}_5$ flakes. Because of its lamellar structure, RTO represents a promising candidate for obtaining really thin samples. By using this technique, several samples have been exfoliated. Most of them present a thickness close to 300 nm. The limit of this technique has not yet been assessed and thinner samples may be feasibly obtained after mastering the technique.

Exfoliated RTO has been characterized through Raman spectroscopy measurements. A possible dependence of the collected Raman signal with respect to the RTO thickness has been studied. The results have shown that, rather than the thickness, the determining factor is the hydration level of the crystal. As a matter of fact, RTO nanocrystals have exhibited a strong sensitivity to moisture, because of superior water absorption. Also, spectra of hydrated flakes have shown similar features to those of annealed crystals presented in [3], pointing towards the role of water absorption as main cause of the changes with respect to spectra of as-grown crystals.

Finally, after device fabrication, $I - V$ measurements have been conducted on one sample, an RTO nanocrystal with size $25 \mu\text{m} \times 5 \mu\text{m} \times 800 \text{nm}$. Some preliminary results have been obtained. In particular, resistivity values $\sim 10^5 \Omega\cdot\text{cm}$, in agreement with previous findings [3], have been estimated. These measurements confirmed the critical role played by water in dictating charge conduction in solid state electrolyte RTO, in agreement with what already demonstrated in [28]. Nonetheless, the analysis of the electrical properties of RTO exfoliated flakes is too immature to give a meaningful interpretation of what observed in the $I - V$ characteristics.

4.2 Future perspectives

I presented here a first approach to investigate the properties of $\text{Rb}_2\text{Ti}_2\text{O}_5$ at the nanoscale. A deep interest in carrying on with the analysis of its physical and electrical properties comes from the preliminary yet noticeable results obtained in this work.

Investigation of novel exfoliation techniques may open new possibilities in terms of shape, thickness and local crystalline structure of RTO flakes or even to obtain nanosheets. Further research in this direction may even unveil new physical properties and give some more insights on the precise charge transport mechanism, still not fully understood.

Bibliography

- [1] R. Carter, A. Cruden and P. J. Hall, "Optimizing for Efficiency or Battery Life in a Battery/Supercapacitor Electric Vehicle," in *IEEE Transactions on Vehicular Technology*, vol. 61, no. 4, pp. 1526-1533, May 2012, doi: 10.1109/TVT.2012.2188551.
- [2] S. Andersson, A. Wadsley, "The crystal structure of $K_2Ti_2O_5$ ", *Acta Chem. Scand.* 15 (1961). Pages: 663-669. doi : 10.3891/acta.chem.scand.15-0663
- [3] R. Federicci, S. Holé, A.F. Popa, L. Brohan, B. Baptiste, S. Mercone, B. Leridon, $Rb_2Ti_2O_5$: superionic conductor with colossal dielectric constant, *Phys. Rev. Mater.* 1 (2017) 032001, <https://doi.org/10.1103/PhysRevMaterials.1.032001>.
- [4] Simon, P., Gogotsi, Y. Materials for electrochemical capacitors. *Nature Mater* 7, 845-854 (2008). <https://doi.org/10.1038/nmat2297>
- [5] Simon P., Gogotsi Y., Dunn B.. (2014). Where Do Batteries End and Supercapacitors Begin?. *Science* (New York, N.Y.). 343. 1210-1. 10.1126/science.1249625.
- [6] Maier, J. Nanoionics: ion transport and electrochemical storage in confined systems. *Nature Mater* 4, 805-815 (2005). <https://doi.org/10.1038/nmat1513>
- [7] G. Binnig, C. F. Quate, Ch. Gerber, Atomic Force Microscope. *Phys. Rev. Lett.* 56, 930-933 (1986). doi: 10.1103/PhysRevLett.56.930
- [8] *Handbook of Micro/Nanotribology*, 2nd edn., ed. by B. Bushan (CRC, Boca Raton 1999), pp.81-144
- [9] "What is Atomic Force Microscopy (AFM)", Nano and more, <https://www.nanoandmore.com/what-is-atomic-force-microscopy>
- [10] Mosca, S., Conti, C., Stone, N. et al. Spatially offset Raman spectroscopy. *Nat Rev Methods Primers* 1, 21 (2021). <https://doi.org/10.1038/s43586-021-00019-0>
- [11] RAMAN, C., KRISHNAN, K. A New Type of Secondary Radiation. *Nature* 121, 501-502 (1928). <https://doi.org/10.1038/121501c0>
- [12] M. Tournoux, R. Marchand, L. Brohan, Layered $K_2Ti_4O_9$ and the open metastable $TiO_2(B)$ structure, *Progress in Solid State Chemistry*, Volume 17, Issue 1, 1986, Pages 33-52, ISSN 0079-6786, [https://doi.org/10.1016/0079-6786\(86\)90003-8](https://doi.org/10.1016/0079-6786(86)90003-8).
- [13] Shripal, Badhwar, S., Maurya, D. et al. Dielectric and a.c. conductivity studies in pure and manganese doped layered $K_2Ti_4O_9$ ceramics. *J Mater Sci: Mater Electron* 16, 495-500 (2005). <https://doi.org/10.1007/s10854-005-2723-4>
- [14] Vikram, S. V., Phase, D. M. & Chandel, V. S. (2010). *J. Mater. Sci. Mater. Electron.* 21, 902-905.
- [15] Andersson, S. & Wadsley, A. D. (1960). *Nature*, 4736, 499-500.
- [16] Andersson, S. & Wadsley, A. D. (1961). *Acta Chem. Scand*, 3, 663-669.
- [17] Wang, Q., Guo, Z. & Chung, J. S. (2009). *Chem. Commun.* 35, 5284-5286. DOI <https://doi.org/10.1039/B909455E>
- [18] Wang, Q., Chung, J. S. & Guo, Z. (2011). *Ind. Eng. Chem. Res.* 50, 8384-8388.
- [19] Schmitz-Dumont, O. & Schulz, A. H. (1952). *Monatsh. Chem.* 83, 638-649.

- [20] Schmitz-DuMont, O. & Reckhard, H. (1959). *Monatsh. Chem.* 90, 134–142.
- [21] R. Federicci, B. Baptiste, F. Finocchi, F. Popa, L. Brohan, K. Béneut, P. Giura, G. Rousse, A. Descamps-Mandine, T. Douillard, A. Shukla, B. Leridon, The crystal structure of $\text{Rb}_2\text{Ti}_2\text{O}_5$, *Acta Crystallogr. B* 73 (2017) 1142–1150, <https://doi.org/10.1107/S2052520617013646>.
- [22] Rémi Federicci, Stéphane Holé, Vincent Démery, and Brigitte Leridon, "Memory effects in the ion conductor $\text{Rb}_2\text{Ti}_2\text{O}_5$ ", *Journal of Applied Physics* 124, 152104 (2018) <https://doi.org/10.1063/1.5036841>
- [23] Novoselov, K & Castro Neto, Antonio. (2012). Two-dimensional crystals-based heterostructures: Materials with tailored properties. *Physica Scripta*. 2012. 014006. 10.1088/0031-8949/2012/T146/014006.
- [24] Novoselov, Kostya S., et al. "Electric field effect in atomically thin carbon films." *science* 306.5696 (2004): 666-669. 10.1126/science.1102896
- [25] Albrecht, T. R, P. Gruëtter, D. Horne, and D. Rugar. "Frequency Modulation Detection Using High-Q Cantilevers for Enhanced Force Microscope Sensitivity." *Journal of Applied Physics* 69.2 (1991): 668-73.
- [26] Salvatore Timpa. Electric and thermoelectric properties of supported 2D materials. *Materials Science [cond-mat.mtrl-sci]*. Université de Paris 7 - Denis Diderot, 2021. English. <tel-03494450>
- [27] Pizzocchero, F., Gammelgaard, L., Jessen, B. et al. The hot pick-up technique for batch assembly of van der Waals heterostructures. *Nat Commun* 7, 11894 (2016). <https://doi.org/10.1038/ncomms11894>
- [28] Sofia de Sousa Coutinho, David Bérardan, Guillaume Lang, Rémi Federicci, Paola Giura, et al.. Effect of water incorporation on the ionic conduction properties of the solid electrolyte material $\text{Rb}_2\text{Ti}_2\text{O}_5 \cdot (\text{H}_2\text{O})_x$. 2021. <hal-03095184>
- [29] Garcia-Belmonte, Germà & V, Kytin & Dittrich, Thomas & Bisquert, Juan. (2003). Effect of Humidity on the ac Conductivity of Nanoporous TiO_2 . *Journal of Applied Physics*. 94. 10.1063/1.1610805.
- [30] Yao, Yao, Xiangdong Chen, Jinfeng Zhu, Baoqing Zeng, Zuquan Wu and Xiaoyu Li. "The effect of ambient humidity on the electrical properties of graphene oxide films." *Nanoscale Research Letters* 7 (2012): 363 - 363.
- [31] Wei, Qiulong & Liu, Jin & Feng, Wei & Sheng, Jinzhi & Tian, Xiacong & He, Liang & An, Qinyou & Mai, Liqiang. (2015). Hydrated vanadium pentoxide with superior sodium storage capacity. *J. Mater. Chem. A*. 3. 10.1039/C5TA00502G.